

CrossMark
click for updatesCite this: *RSC Adv.*, 2016, 6, 46929

An overview of the structural, textural and morphological modulations of g-C₃N₄ towards photocatalytic hydrogen production

Sulagna Patnaik, Satyabadi Martha and K. M. Parida*

Graphitic carbon nitride (g-C₃N₄) is gaining more and more importance as a photocatalytic material due to its promising electronic band structure and high thermal and chemical stability. Very recently, a variety of nanostructured g-C₃N₄ photocatalysts with varying shapes, sizes, morphologies and electronic band structures have been reported for application in photocatalytic research. This critical review represents an extensive overview of the synthesis of a variety of g-C₃N₄ nanostructured materials with a controllable structure, morphology and surface modification for superior electronic properties. This article highlights the design of efficient photocatalysts for the splitting of water into hydrogen gas using solar energy. Finally, in the summary and outlook, this article highlights the ongoing challenges and opportunities of g-C₃N₄. It is also hoped that this review will stimulate further investigation and will open up new possibilities to develop new hybrid g-C₃N₄ materials with new and exciting applications.

Received 14th December 2015

Accepted 22nd April 2016

DOI: 10.1039/c5ra26702a

www.rsc.org/advances

Centre for Nano Science and Nano Technology, Siksha 'O' Anusandhan University, Bhubaneswar-751030, India. E-mail: kulamaniparida@soauniversity.ac.in; satyabadimartha@soauniversity.ac.in; Fax: +91-674-2350642; Tel: +91-674-2351777

1. Introduction

Photocatalytic water splitting for the production of H₂ energy has become more important in recent decades. The hydrogen evolved from this process is green, environmental friendly and a carbon neutral fuel.¹⁻³ Since the report of Fujishima and



Sulagna Patnaik completed her master's degree at the Regional Engineering College, Rourkela, in 1989 in chemistry. Then, she became a lecturer in chemistry at Rayagada Autonomous College, Odisha, in 1991. She is presently working at Nimapara Autonomous College and pursuing research work at the Centre for Nanoscience and Nanotechnology, SOA University, Bhubaneswar. She has

published one research article in an international journal. Her research work is focused on the development of modified C₃N₄-based photocatalysts for hydrogen energy production and pollution abatement.



Dr Satyabadi Martha completed his Master of Science (M.Sc.) in 2008 from Utkal University, Bhubaneswar. Then, he completed his PhD degree from North Orissa University under the guidance of Prof. Kulamani Parida. His research work is focused on the development of visible light responsive photocatalysts for hydrogen production, CO₂ reduction and pollution abatement. He also

spent 1 year at the School of Energy and Chemical Engineering, UNIST, South Korea, as a postdoc researcher with Prof. Jae Sung Lee. He has published 26 research articles in international journals and three national patents and presented his works in several national and international symposiums and conferences. Currently, he is working as assistant professor at the Centre for Nanoscience and Nanotechnology, ITER, SOA University. Currently, his research work is focused on powder- and film-based semiconductor material for solar fuel production.

Honda about photoelectrochemical hydrogen evolution, many photocatalytic and photoelectrochemical systems have been developed. However, their practical applications are still hindered because of the relatively high cost of photocatalytic H₂ production methods. Therefore, the development of various sustainable semiconducting materials, especially those consisting of earth-abundant elements, has attracted growing attention. Among these, recently developed polymeric g-C₃N₄ is a novel metal-free visible-light-induced organic semiconductor photocatalyst and is considered especially attractive to researchers. It offers a promising high performance due to its hardness, light weight, preparation from easily available starting material, excellent stability at ambient conditions and as it has suitable band gap energy of 2.7 eV and can absorb blue light up to 450 nm.¹ This novel nanostructured material was found to have many potential applications, such as energy conversion, the purification of contaminated water, good performance in the photo-oxidation of dyes,¹ as a base metal-free catalyst for NO decomposition,² as a reference material in differentiating oxygen activation sites for oxidation reactions, as a functional material to synthesise nanosized metal particles and as a stable photocatalyst for H₂ evolution from water under visible light irradiation and also in fuel cells.³⁻⁷

This polymeric derivative carbon nitride (C₃N₄) was first synthesised by Berzelius, and then named by Liebig in 1834⁸ as melon, which is regarded as one of the oldest structures of synthetic polymers. The structure of this compound was first described by Franklin in 1922.⁹ C₃N₄ exists in five different allotropic forms: α-C₃N₄, β-C₃N₄, graphitic-C₃N₄, cubic C₃N₄, and pseudo-cubic-C₃N₄. g-C₃N₄ possesses a stacked 2-dimensional (2D) graphite-like planar structure, with N-heteroatoms



Prof. K. M. Parida is currently working as professor in Chemistry and as Director at the Centre for Nanoscience and Nanotechnology, ITER, Siksha 'O' Anusandhan University, Bhubaneswar. Before coming to ITER, he worked as a Chief Scientist and head of Colloids and Materials Chemistry Department at the CSIR-Institute of Minerals and Materials Technology, Bhubaneswar, Odisha, India, and

Professor at the Academy of Scientific and Innovative Research (AcSIR), New Delhi, India. He is the author of more than 290 international journals and 18 national and international patents as well as three book chapters. His research interest is focused on the design and development of a wide cross section of materials, such as metal oxides, metal phosphates, metal sulfates, cationic and anionic clays, perovskites, zeolites, graphene, C₃N₄ and nano-metal/metal oxide/complex promoted mesoporous materials and naturally occurring materials, such as manganese nodules, manganese nodules leach residue and manganese oxides of natural origin for energy and environmental applications.

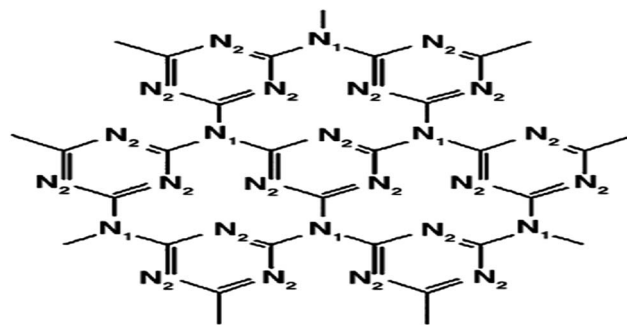


Fig. 1 Structure of planar g-C₃N₄. Nitrogen occupies two positions in the layer, labelled N₁ and N₂ (reproduced from ref. 8).

substituted in the graphite framework containing π-conjugated systems maintaining a distance of 0.326 nm between two layers. g-C₃N₄ is made up of only carbon and nitrogen and is stable in both acidic and basic media due to the presence of strong covalent bonds between the carbon and nitrogen atoms. Bonding consists of a N-atom (N₁) in a planar sp² configuration and a 3-coordinated C-atom, which is sp² hybridised and is bonded to 2-coordinated N-atom (N₂) in a 1,3,5-triazine ring. Both the nitrogen atoms (labelled as N₁ and N₂) are sp² hybridised (Fig. 1). In the molecular crystal, strong covalent bonds exist, but inside the molecular building blocks, there exists weak interactions, such as hydrogen bonding and van der Waals forces.¹⁰ As a semiconductor material with a suitable bandgap, g-C₃N₄ absorbs visible light to cause photoexcitation, leading to a spatial charge separation between the electron in the CB and hole in the VB, which can take part in subsequent redox reactions with the surface adsorbed molecules to yield the ultimate products. The N-atoms are the preferred oxidation sites and the C-atoms provide the reduction sites.

Due to the different degree of condensation, the polymerized structure of g-C₃N₄ develops optimization in its packing, which makes the material behave as a multifunctional catalyst. The presence of a π-conjugated system, as shown in Fig. 2, modifies its bulk electronic structure and surface properties to allow it to exhibit:¹¹

- Electronic properties;
- Nucleophilic properties;
- The ability to form H-bonds;
- Photocatalytic activity.

Through its special electronic properties, it can activate the Friedel-Craft reaction, Diels-Alder reactions and the

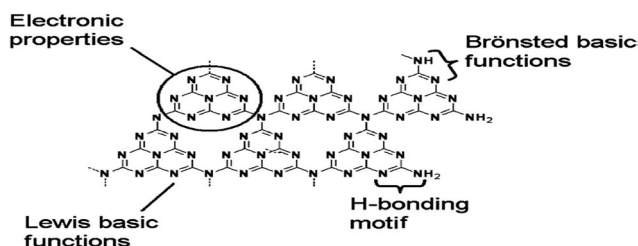


Fig. 2 Structure of planar g-C₃N₄ (reproduced from ref. 11).

trimerisation of alkynes.¹² Due to its nucleophilic properties, it helps in the activation of CO₂.¹³ Its ability to form H-bonds favours the trimerization of nitrides.

2. g-C₃N₄ as a photocatalyst

g-C₃N₄ has been identified as an efficient visible-light-active polymeric semiconductor photocatalyst for photochemical reactions due to its unique electronic band structure for both water reduction and oxidation. When g-C₃N₄ receives photon energy $\geq E_g$ (bandgap = 2.7 eV) from a light source, electrons are excited from the valence band (VB) to the conduction band (CB), leaving a corresponding number of holes in the valence band. It is said to be in its photoexcited state when this results in electron (e⁻)-hole (h⁺) pairs. These excited charge carriers (electrons and holes) act as highly reactive species with robust reducing and oxidizing capacities.^{10,11} They may recombine or get trapped in metastable surface states or can react with suitable electron acceptors/donors adsorbed on the surface of the catalyst. In the case of common photocatalysts in the bandgap region, no energy levels are available. This allows a delay in the recombination of electron-hole pairs because of the void energy region (bandgap). Efficient electron-hole separation and fast charge transport restricts the bulk and surface charge recombination, which is essentially required for the photogenerated charge carriers to migrate to the surface reaction sites. Due to the migration of the photoexcited electrons and holes to the active sites on the surface, they can split water into hydrogen and oxygen, depending on the sacrificial agent used. The surface properties of g-C₃N₄ intrinsically favour the separation and transfer of charge carriers by generating surface states where electrons and holes are spatially trapped and transferred for subsequent redox reactions, as shown in Scheme 1.

2.1. Disadvantages of g-C₃N₄ as a photocatalyst¹⁴⁻¹⁷

Various theoretical techniques such as molecular dynamics methods, first principle pseudopotentials, routines based on Hartree-Fock and local density approximations, *etc.* have been applied to study different forms of carbon nitrides. g-C₃N₄ is the most stable allotrope among various carbon nitride compounds

and has attracted much attention due to its potential application in splitting water and decomposing organic pollutants under visible light. However, its photocatalytic activity is non-satisfactory due to:¹⁸⁻²¹

- (1) Its low quantum efficiency, due to fast recombination of the photogenerated the electron-hole pairs;
- (2) Pure g-C₃N₄ can absorb only blue light in the solar spectrum (450 nm), which limits the utilization of a broad spectrum of solar light;
- (3) During synthesis, the high degree of condensation of the monomers renders the materials with a low surface area ($\sim 10 \text{ m}^2 \text{ g}^{-1}$) and without forming textured pores;
- (4) The grain boundary effect, which disrupts the delocalization of electrons from the surface of a photocatalyst through the interface.

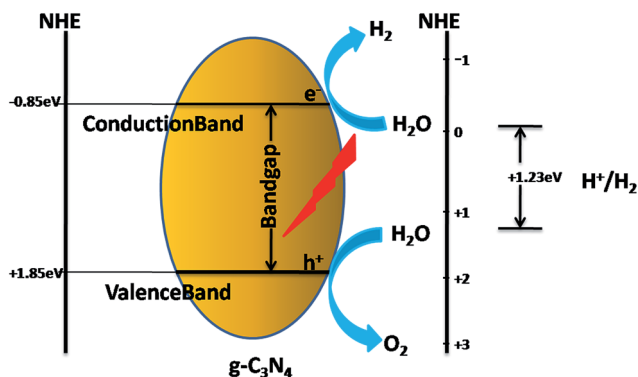
2.2. Steps to overcome the limitations

To take better advantage of g-C₃N₄, it is important to optimize the material to explore more efficient photocatalytic reactivity. The design of high-performance g-C₃N₄ is highly dependent on the size, morphology, surface area, abundant surface active sites and even extended light harvesting capacity. Some of the important strategies to improve the photocatalytic hydrogen production of g-C₃N₄ are *via*:

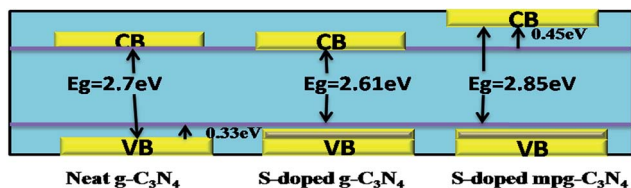
- (i) Preparation of mesoporous and ordered mesoporous g-C₃N₄;²²⁻³⁸
- (ii) Preparing texturally and morphologically controlled g-C₃N₄;³⁹⁻⁴⁵
- (iii) Doping with non-metals, such as B, S, P, F, I, *etc.*;⁴⁶⁻⁵⁸
- (iv) Loading co-catalysts (especially noble metals, such as Ag, Pt, Au, *etc.*);⁵⁹⁻⁷⁹
- (v) Preparing heterojunction/composites with transitional metal-/metal oxide-based materials.⁸⁰⁻⁹⁶

In order to absorb light effectively in the whole visible spectrum, the bandgap of the photocatalyst should correspond well to the wavelength of the irradiated light. Here, in this review, we discuss some of the methods, giving special emphasis to heteroatom doping, loading a co-catalyst, designing composites/heterojunctions, *etc.*, which can effectively alter the electronic band structure as well as the redox potential of g-C₃N₄ in order to extend the light absorption and to promote photocatalytic hydrogen generation in the visible region.

Heteroatom doping mainly involves the incorporation of atoms or ions into a crystalline lattice, and modifies the bulk structure of crystallites. Doping with non-metals reduces the energy gap to enhance the visible light absorption of g-C₃N₄. The increased dispersion of the contour distribution of the HOMO and LUMO brought about by doping facilitates the charge carrier mobility and favours the charge separation. The wider the VB, the higher the mobility of the generated holes, and this thus improves the photo-oxidation efficiency of the holes. To increase the VB width by non-metal doping, the dopant atom must have a lower electronegativity than the substituted atom and there must be a homogeneous distribution of the dopant. The mechanism behind the enhanced



Scheme 1 Charge transfer mechanism of neat g-C₃N₄ as a photocatalyst.

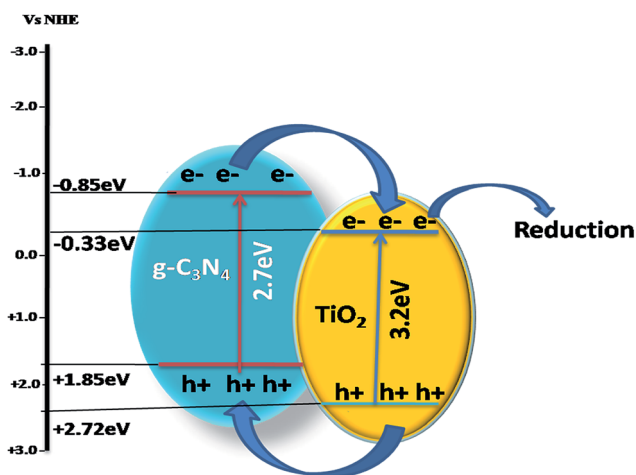


Scheme 2 Upliftment of the band edge in S-doped $g\text{-C}_3\text{N}_4$.

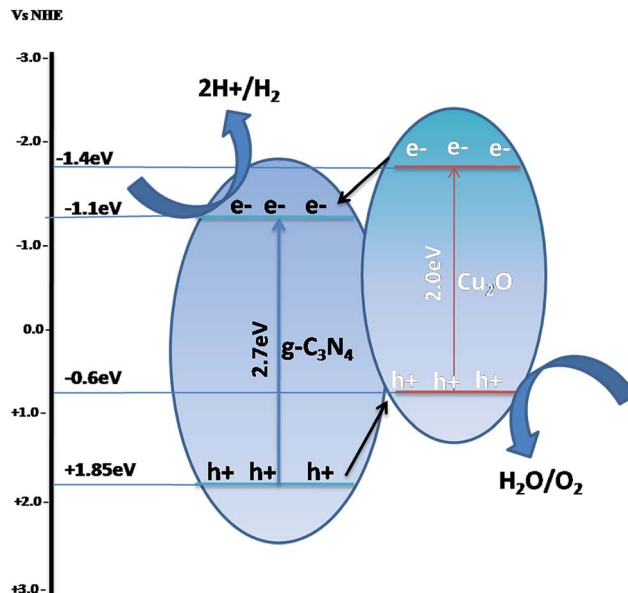
activity is explained in the photocatalytic Scheme 2, taking the example of S-doped $g\text{-C}_3\text{N}_4$. Liu *et al.*⁵⁵ reported S-doped mpg- C_3N_4 with a unique electronic structure that showed an increased VB width along with an elevated CB minimum and a slightly reduced absorbance, and its photoreactivity for H_2 evolution increased 7.2 to 8.0 fold. Whereas, Hong *et al.*⁵⁶ reported an upliftment of VB and a decrease in the bandgap to 2.61 eV by *in situ* S-doping for increased activity (H_2 evolution increased 30-fold).

Semiconductor hybridization and the creation of heterojunctions/composites with an appropriate semiconducting material is another effective strategy to broaden the utilization of $g\text{-C}_3\text{N}_4$ for visible light photocatalytic hydrogen generation. This is based on the band alignment between $g\text{-C}_3\text{N}_4$ and the other semiconductors to achieve a better efficiency for photogenerated charge separation and to promote photocatalytic activity. This promotion effect was explained by creating heterojunctions by using three different mechanisms, as described below.

(1) Though sensitization, in which electrons generated by visible light irradiation in $g\text{-C}_3\text{N}_4$ migrate to a wider bandgap semiconductor with a VB and CB at a higher potential (such as in ZnO , TiO_2 , *etc.*, which is explained further in the later part of this review), while the photogenerated electrons from the CB of $g\text{-C}_3\text{N}_4$ are transferred to the CB of wider bandgap semiconductors, as shown in Scheme 3, and help in photoreduction



Scheme 3 Charge transfer mechanism in a heterojunction of $g\text{-C}_3\text{N}_4$ with a wider bandgap semiconductor with both VB and CB at a higher potential.



Scheme 4 Charge transfer mechanism in a heterojunction of $g\text{-C}_3\text{N}_4$ with narrow-bandgap semiconductors with a VB and CB at lower potentials.

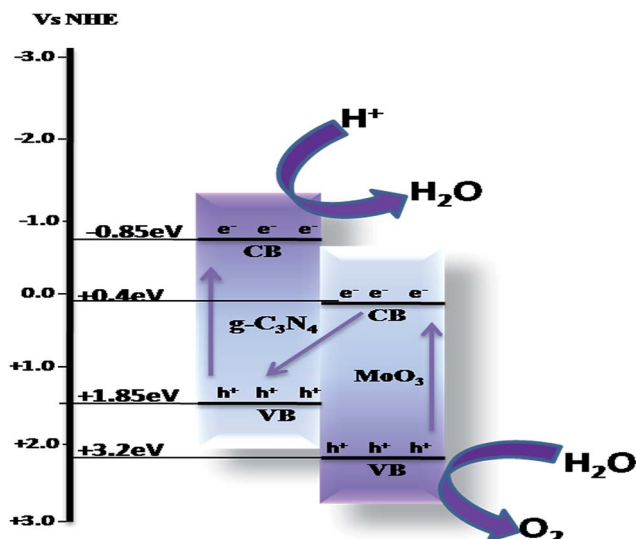
and the holes are transferred to the CB of $g\text{-C}_3\text{N}_4$, thus resulting in effective charge separation.

(2) *Via* a heterojunction/composite photocatalyst, in which both semiconductors are visible light active and can be excited to form electron–hole pairs. The photogenerated electrons migrate from Cu_2O with a higher CB to another semiconductor with a lower CB, while the photogenerated holes migrate from $g\text{-C}_3\text{N}_4$ with a lower VB to another semiconductor (Cu_2O) with a higher VB, as shown in Scheme 4. The double charge transfer may also lead to the separation of electrons and holes and enhance the photocatalytic efficiency.

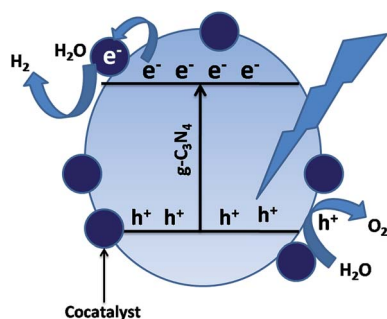
(3) Through a direct Z-scheme type mechanism, in which the photogenerated electrons migrate in a Z-scheme route and greatly affect the band edge potentials of the semiconductors. The photogenerated electrons from a semiconductor with a lower CB recombine with photogenerated holes from the $g\text{-C}_3\text{N}_4$ with a higher VB. Meanwhile, the photogenerated electrons with strong reducibility were left on the semiconductor with higher CB, and the holes with strong oxidizability were left on the semiconductor with a lower VB, as shown in Scheme 5. These photogenerated electrons and holes could participate in the photocatalytic process.

Although all the three mechanisms have been widely used by different groups of scientists to explain their works, the band edge potential of the semiconductor is generally considered as the key factor to choose the mechanism most suitable for the specific research.

$g\text{-C}_3\text{N}_4$ /co-catalyst hybrids with noble metal co-catalysts, such as Pt, Au, Ag, *etc.*, have improved interfacial contact, which helps to capture the conduction-band electrons for photocatalytic hydrogen generation. Nanoparticles of noble metals can strongly absorb visible light due to their surface



Scheme 5 Photocatalytic charge transfer by a Z-scheme mechanism.



Scheme 6 Photocatalytic charge transfer by co-catalyst loading.

plasmon resonance, which can be tuned by varying their shape, size and surroundings. When the surface of the photocatalyst is loaded with the noble metals, the photogenerated electrons migrate to the surface of the photocatalyst and are transferred easily to the noble metal co-catalyst, as in Scheme 6, because the Fermi levels of noble metals lie at a lower potential than that of the semiconductor photocatalyst. The performance of $g\text{-C}_3\text{N}_4$ can be significantly improved by the use of co-catalysts, such as Pt, Ru, Rh and Ni, which are often employed as co-catalysts in energy storage processes. In the case of photocatalytic hydrogen evolution, the co-catalysts are usually considered as electron traps, thus delaying the charge recombination process and making electrons and holes readily available for the photocatalytic process and acting as thermal redox active centres. Several other factors, such as the choice of the sacrificial agent, the intensity of the light source, the pH of the solution and the loading procedure also affect the performance of the co-catalyst.

3. Synthesis of neat $g\text{-C}_3\text{N}_4$

Different groups of scientist have reported various methods to modify the structure, morphology and texture of neat $g\text{-C}_3\text{N}_4$

material by synthesizing nanopowders, nanosheets, nanowires (or nanorods), nanobelts, nanotubes and nanospheres.

3.1. $g\text{-C}_3\text{N}_4$ nanopowder

This material is of great interest because of the fact that it can be synthesized from easily available and cost-effective starting materials, such as cyanamide, dicyandiamide, melamine, urea, cyanurichloride, 2-amino-4,6-dichlorotriazine, *etc.*, by a facile pyrolysis method.^{12,13} The graphitic- C_3N_4 synthesized from various amine precursors develops different degrees of photocatalytic efficiency. Zhang *et al.*²² prepared $g\text{-C}_3\text{N}_4$ by heating cyanamide, dicyanamide and melamina in an alumina crucible with a cover to maintain a semi-closed atmosphere to prevent sublimation. The obtained yellow coloured polymer was $g\text{-C}_3\text{N}_4$ nanopowder. The optical and electronic properties of $g\text{-C}_3\text{N}_4$ are dependent on the C/N ratio and the degree of condensation. The degree of condensation is also dependent on the temperature and starting material. In the case of melamine, the morphology of the products was changed from spherical nanoparticles into layered carbon nitride and graphitic- C_3N_4 with the increase in temperature. The products were maintained in the crystalline melamine phase when the heating temperature was lower than 300 °C.²² When the temperature increased gradually, it was transformed into crystalline or amorphous graphite-like C_3N_4 compounds, and the morphology of the product also changed (Table 1).

The major limitation in the synthesis of $g\text{-C}_3\text{N}_4$ is its easy sublimation at elevated temperatures. Its easy sublimation can be suppressed to a large extent if the melamine co-exists with others species where H-bridges are present. The synthesis of $g\text{-C}_3\text{N}_4$ from melamine mainly involves a combination of a polyaddition and polycondensation. Polycondensation proceeds *via* the elimination of NH_3 molecules (Fig. 3).²³ During polymerization, melamine first forms a C_3N_4 sheet structure based on triazine units, which on subsequent polymerization forms a C_6H_8 sheet structure based on tri-s-triazine units.

Mechanism of the synthesis. Triazine (Fig. 4a) and tri-s-triazine (Fig. 4b) differ in their stabilities due to the different electronic environments around the edge N-atoms and size of the nitride pores. During the formation of the tri-azine structure, the energy of the system increases due to repulsion between the lone pairs of electrons on the edged N-atoms. Therefore, the linear chain is strongly buckled to form a tri-s-triazine molecule in order to maximize the distance between the N-atoms on the edge. This buckling increases the N–N distance from 2.44 Å to 2.52 Å, which decreases the N–N repulsion, and the energy decreases by 11 kJ mol^{-1} .^{24,25}

Table 1 Effect of temperature on the morphology

| Temperature | Morphology | Particle size | Structure |
|-------------|------------|-----------------------|--------------------------|
| 300 °C | Granular | 50–80 nm | Crystalline |
| 350–400 °C | Layered | 0.5–0.8 μm | Crystalline or amorphous |
| 500 °C | Sheet-like | 0.5–1.0 μm | Completely amorphous |
| 600 °C | Flakes | 0.5–1.5 μm | Amorphous |

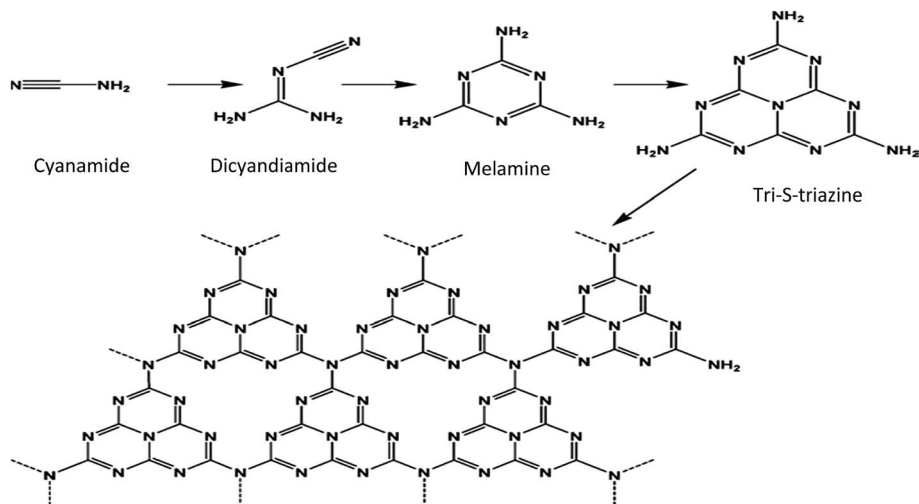


Fig. 3 Mechanism of the synthesis of $g\text{-C}_3\text{N}_4$ (reproduced from ref. 11).

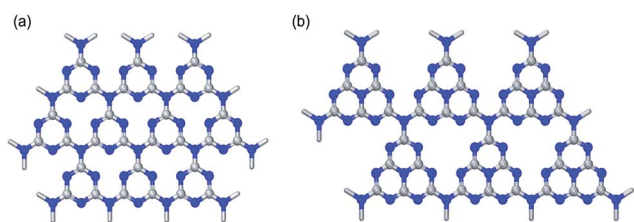


Fig. 4 Representation of (a) triazine and (b) tri-s-triazine (reproduced from ref. 27).

3.2. $g\text{-C}_3\text{N}_4$ mesoporous

Nanomaterials should have a large specific surface area as the most important requirement to be effective in photocatalytic applications. It has been found that an additional important feature of nanomaterials for photocatalytic applications is their porous morphology.^{28–38} Recently, various nanostructured $g\text{-C}_3\text{N}_4$ materials with a mesoporous and highly ordered porous network with a large specific surface area and optimum pore size have been developed. $g\text{-C}_3\text{N}_4$ nanopowder obtained by the thermal polycondensation of various nitrogen-rich starting materials results in bulk materials with a low surface area ($\sim 10\text{ m}^2\text{ g}^{-1}$). Low surface area has become one of the main disadvantage hindering the wide potential application of this new emerging material. This is because surface area plays an important role in photochemical reactions by offering more active sites. Porous materials have drawn much attention as heterogeneous catalysts for energy conversion due to their porosity and large surface area.^{26–31} Mesoporous $g\text{-C}_3\text{N}_4$ shows unique semiconductor properties, along with a large surface area and accessible crystalline pore walls, for mass transfer as a promising metal-free photocatalyst. As compared to the bulk $g\text{-C}_3\text{N}_4$, mpg- C_3N_4 material exhibits a higher specific surface area of up to $830\text{ m}^2\text{ g}^{-1}$ and a larger porosity of up to $1.25\text{ cm}^3\text{ g}^{-1}$.³² The most important pathways for the preparation of meso- $g\text{-C}_3\text{N}_4$ are based on templating

methods, such as soft templating (self-assembly) and hard templating (nanocasting) methods. In the soft templating method, the porosity is introduced by the co-operative assembly often being carried out under hydrothermal conditions. The most commonly used soft templates are Triton-X-100, P123, F127, Brij30, Brij58 and Brij76, to obtain different pore structures and specific surface areas.³³ The preparation of self-porous materials by soft templates is still very difficult. In the case of $g\text{-C}_3\text{N}_4$, the practical problem is that the condensation to form polymeric CN-structures takes place around or above the decomposition temperature of the commonly used soft templates. However, by using primary nanopores in the silica template,^{34,35} nanostructured $g\text{-C}_3\text{N}_4$ in the form of nanowires/nanospheres can be replicated to form stable replica arrays. After removal of the template, the desired nanoporous $g\text{-C}_3\text{N}_4$ is obtained, which is an inverse replica of the silica template. Groenewolt *et al.*³⁸ prepared mpg- C_3N_4 nanoparticles using mesoporous silica as the hard template. The most commonly used hard templates are silica nanoparticles, 2D hexagonal SBA-15 and 3D cubic KIT-6, IBN-4, *etc.* Mesoporous- C_3N_4 , when synthesized by using silica nanoparticles as the hard template, has an increased specific surface area but there is a decrease in crystallinity, which acts against effective excited charge separation. Therefore, enhancement of the crystallinity of the $g\text{-C}_3\text{N}_4$ polymer and, at the same time, the surface area is still a challenge. Also, the silica nanoparticles can be removed by using aqueous NH_4HF_2 or HF, which is hazardous and not environmentally friendly. Synthesizing ordered mesoporous $g\text{-C}_3\text{N}_4$ results in a large external surface and improves the activity of the photocatalyst.³¹ By using ethylenediamine and CCl_4 as the precursor and SBA-15 as a template, ordered mesoporous carbon nitride can be prepared. The ompg- C_3N_4 maintains the rod-like morphology of the SBA-15 template. Also, the surface area increases to $239\text{ m}^2\text{ g}^{-1}$.^{32,33} Recently various template-free methods have been explored to overcome the difficulties in the removal of the template.

3.3. g-C₃N₄ nanorods

Most researchers found that g-C₃N₄ has a nanoporous or nanosphere morphology. It has been reported that the synthesis of g-C₃N₄ nanorods involves the transformation process of g-C₃N₄ from nanoplates to nanorods. The dimensionality and size of the material have been regarded as critical factors to enhance the photocatalytic activity. g-C₃N₄ nanorods can be synthesized with well-controlled dimensionality by removing the surface defects and producing more active lattice faces to enhance the photocatalytic activity significantly. Bai *et al.*³⁹ prepared g-C₃N₄ nanorods by a simple reflux method, which increased the number of active lattice faces by eliminating surface defects. The morphology and the crystal growth of the products were controlled by changing the reaction time and reactant solvent concentration.

3.4. g-C₃N₄ nanosheets

g-C₃N₄ nanosheets are obtained by the exfoliation of bulk g-C₃N₄. For the synthesis of nanosheets, bulk g-C₃N₄ was suspended in different types of solvents, such as IPA, *N*-methyl pyrrolidone (NMP), water, ethanol and acetone. Then, the dispersion was subjected to sonication at room temperature. There followed a gradual exfoliation of the material to form g-C₃N₄ nanosheets with the increase in sonication time. Yang *et al.*⁴⁰ exfoliated g-C₃N₄ by using isopropanol (IPA) to form g-C₃N₄ nanosheets (Fig. 5) of ~2 nm thickness. However, the use of inorganic solvents or water for the sonochemical exfoliation method suffers from a long ultrasonic treatment required and results in a low exfoliation efficiency. Cheng *et al.*⁴¹ reported the

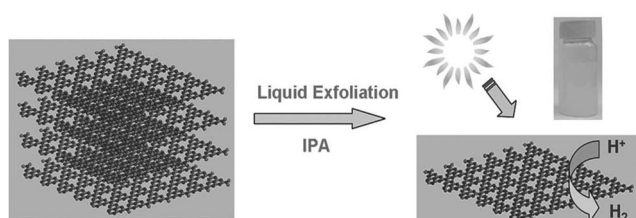


Fig. 5 Fabrication of nanosheets of g-C₃N₄ by the liquid exfoliation method from g-C₃N₄ powder (reproduced from ref. 40, licence number 3767461234354).

formation of a stable colloid of g-C₃N₄ nanosheets of ~9 nm thickness on a large scale following a H₂SO₄ exfoliation route.

3.5. Structure-distorted g-C₃N₄ nanosheets

Chen *et al.*⁴² reported the formation of structure-distorted g-C₃N₄ nanosheets (Fig. 6) by thermal etching, and the structure showed extended optical absorption in the visible region. Due to the distortion, the g-C₃N₄ nanosheets were formed. These distorted nanosheets reduce the repulsive interactions between the lone pairs of electrons present in the N-atoms. The distortion is possible when the condensation temperature is gradually increased higher than 550 °C (550, 600, 625, 650, 675 and 700 °C) and maintained for 2 h at the final temperature.

3.6. g-C₃N₄ hollow nanospheres

Zheng *et al.*^{43,44} designed a hollow carbon nitride nanosphere by grafting an organic group into the structure of g-C₃N₄ to extend the pi-conjugation and to enhance its photocatalytic activity for hydrogen evolution. During polymerization, ATCN (2-aminothiophene-3-carbonitrile) was added to cyanamide as the precursor. In the product, the thiophene groups are grafted in place of amino groups by nucleophilic reaction. A similar carbon nitride nanospheres network was also obtained by using some other organic compounds, such as barbituric acid and 2-aminobenzonitrile. Zheng *et al.*⁴⁴ designed hollow carbon nitride nanospheres (HCNS) by using silica spheres as the template. After removal of the template by using NH₄HF₂, a highly stable polymeric semiconductor material was obtained. Bai *et al.*⁴⁵ also designed hollow g-C₃N₄ nanospheres by using silica spheres as the template in a solvothermal technique.

3.7. Synthesis of non-metal-doped g-C₃N₄ (C, B, F, S, P, I, etc.)

Chemical doping is an effective strategy to modify the electronic structure of g-C₃N₄. Heteroatoms have been used to shift the optical absorption in the visible region by creating localized/delocalized states in the bandgap. Both the composition and the properties of g-C₃N₄ can be further engineered by introducing some non-metallic elements, such as N, C, B, F, S, P, I, etc.^{46–58} into the matrix in order to modify the molecular structure.

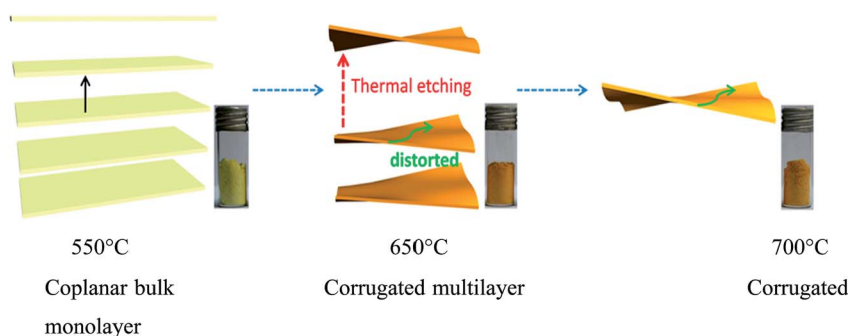


Fig. 6 Fabrication structure of distorted carbon nitride nanosheets (reproduced with permission from ref. 42, Copyright American chemical society, 2014).

Wang *et al.*⁴⁷ synthesized fluorinated polymeric g-C₃N₄-solids (CNF) by directly incorporating NH₄F as the doping reagent during the condensation process of classical g-C₃N₄. By incorporating different amounts of NH₄F, the fluorine concentration in the resulting CNFs can be controlled. Lin *et al.*⁴⁸ reported fluorine-doped g-C₃N₄ by using BimBF₄ and urea. Wang *et al.*⁴⁹ synthesized B-doped g-C₃N₄ (CNB) by using BH₃NH₃ as a molecular doping source during the condensation process rather using oxygen-containing precursors or the generation of HF. The resulting^{50,51} CNB materials were found to have a potential oxidation strength. B-Doped g-C₃N₄ can also be prepared by substituting the H-atom at the terminal of the melon structure with boron, forming C-NB and C-NB₂ functional groups. Yan *et al.*⁵¹ synthesized B-doped g-C₃N₄ by heating a mixture of melamine and boron oxide. Zhang *et al.*⁵² reported the synthesis of P-heteroatom doped polymeric g-C₃N₄ by co-condensation between dicyandiamide and a phosphorous containing ionic liquid. 1-Butyl-3-methylimidazolium hexafluoro phosphate (BmimPF₆) is the most common ionic liquid used as a mild P-source for doping polymeric g-C₃N₄ as they are thermally stable during the polycondensation. With an increase in temperature, PF₆⁻ is expected to react with the amine groups to join the C-N framework. The P-atom is found to be homogeneously distributed on the surface of the doped g-C₃N₄ solid. Dong *et al.*⁵³ synthesized carbon self-doped g-C₃N₄ by using melamine pre-treated with absolute ethanol as the precursor to provide more carbon, whereas Zhang *et al.*⁵⁴ reported the synthesis of carbon self-doped g-C₃N₄ by the thermal condensation of dicyandiamide with barbituric acid. Liu *et al.*⁵⁵ synthesized sulphur-doped g-C₃N₄ by the post-treatment of pristine g-C₃N₄ at 450 °C in a gaseous H₂S atmosphere. Besides this, sulphur can also be doped into the g-C₃N₄ matrix⁵⁶ by using sulphur-enriched trithiocyanaric acid as the precursor *via* a polycondensation process using post-treatment, where the terminal -SH groups act as the leaving group. Hong *et al.*⁵⁶ synthesized mesoporous-S-g-C₃N₄ from thiourea using SiO₂ nanoparticles as the hard template. During the copolymerisation, the C-N network is converted into a S-N bond. Zhang *et al.*⁵⁷ synthesized I-g-C₃N₄ by using dicyandiamide and iodide ion as the carbon nitride source and dopant (a facile *in situ* method). Wang *et al.*⁵⁸ synthesized B- and F-enriched mesoporous g-C₃N₄ by using a simple soft template, such as ionic liquid, 1-butyl-3-methylimidazolium tetrafluoroborate (BmimBF₄). Due to its special solvent structure, BmimBF₄ is an interesting solvent in the synthesis of nanoparticles derived from the ion-ion interaction and tendency to form hydrogen bonding.

3.8. Synthesis of noble-metal-loaded g-C₃N₄

Although g-C₃N₄ is a good photocatalyst, its application is limited due to electron-hole recombination. To make it chemically productive, different precious noble metal species, such as Ag,⁵⁹⁻⁶⁴ Pt,^{65,66} Rh,⁶⁷⁻⁶⁹ Au,⁷⁰⁻⁷⁴ Pd⁷⁵⁻⁷⁹ and RuO₂, must be used as co-catalysts to increase the separation of photoinduced charge carriers from the bulk to the surface, in order to enhance the production of H₂ gas by the splitting of water. These co-

catalysts usually act as electron traps to prevent charge recombination and to enhance the rate of the photocatalytic process.

Zhang *et al.*⁵⁹ synthesized Ag₃PO₄-g-C₃N₄ bulk heterojunctions by mixing g-C₃N₄, Na₂HPO₄ and AgNO₃ solution following an ion-impregnating method. Jiang *et al.*⁶⁰ reported the formation of Ag₂S-g-C₃N₄ composite photocatalysts *via* a simple precipitation method by using g-C₃N₄, AgNO₃ solution in ethanol and thioacetamide (TAA). Platinum can be loaded on the surface of the catalyst either by the impregnation method or by photodeposition or by reduction. Chen *et al.*³¹ reported the synthesis of Pt-doped g-C₃N₄ by using H₂PtCl₄ and g-C₃N₄ as the precursor by a photodeposition technique. Pt catalysts supported on carbon nitride nanotubes were prepared by Zeng *et al.*⁶⁵ with a borohydride reduction method. Zhang *et al.*⁶⁷ synthesized a Rh-g-C₃N₄ composite by a photodeposition method using PVP (polyvinyl pyrrolidone), with the Rh nanoparticles in the range of 4–9 nm prepared by the polyol reduction method. To control the particle size, PVP (polyvinyl pyrrolidone) was used as a capping agent. For the preparation of Rh nanoparticles, RhCl₃ · nH₂O salt is preferably used, but to get comparatively bigger nanoparticles Rh(III), acetylacetonate Rh(acac)₃ is used in THF (tetrahydrofuran). Then, these nanoparticles are incorporated in g-C₃N₄ by photodeposition by adding a suspension of Rh nanoparticles in a dropwise manner to a suspension of g-C₃N₄ in glycerol. Samanta *et al.*⁷⁰ prepared Au-g-C₃N₄ by the deposition-precipitation method by using HAuCl₄, urea solution and g-C₃N₄ powder as the precursor. In another way, Au-g-C₃N₄ nanocomposites were prepared by Chang *et al.*⁷¹ by a facile citrate-reduction method using HAuCl₄, sodium citrate solution and g-C₃N₄ as the precursor. Chang *et al.*⁷⁵ fabricated palladium-modified mesoporous graphitic carbon nitride polymer (Pd/mpg-C₃N₄) by mixing an equal volume of PdCl₂ solution to mpg-C₃N₄ under vigorous magnetic stirring, followed by the addition of KBH₄.

3.9. Synthesis of transitional metal- and metal oxide-promoted g-C₃N₄

Noble metals, such as Au, Pt, Pd, Rh and Ag, are very effective for trapping the photogenerated electrons, thus helping to improve the separation of charge carriers. However, the high cost of noble metals restricts their practical applications. The optical and electronic properties of g-C₃N₄ could also be modified by incorporating a transition metal into the network of g-C₃N₄. Transition metal loading is helpful for modification of the electronic properties of g-C₃N₄ and can extend its optical absorption in the visible region, which enhances the photocatalytic performance.⁸⁰⁻⁹⁷ Transition metal-based heterojunctions of g-C₃N₄ can be prepared by mixing transitional metal salts of Fe(III), Cu(II), Zn(II), *etc.* with the precursor of g-C₃N₄ by a co-thermal condensation.

3.10. Synthesis of composites of g-C₃N₄ with wide-bandgap semiconductors

Various composites and heterojunctions of g-C₃N₄ with transitional metal ions and transition metal oxides have been reported with good photocatalytic activity. However, most of the

transition metal oxides (with wide-bandgap energy) are only ultraviolet (UV) light active. To make them visible light active ($420 \text{ nm} < \lambda < 800 \text{ nm}$) with a bandgap less than 3 eV and practically useful for photocatalysis, the wide-bandgap transition metal oxides are tailored towards the visible region by coupling them with graphitic carbon nitride. Herein, we present a systematic overview on the synthesis of some such wide-bandgap transitional metal oxide semiconductors.

Sun *et al.*⁸⁰ prepared g-C₃N₄-ZnO composite from melamine and Zn(CH₃COO)₂ by direct calcinations at 520 °C. In the case of g-C₃N₄-ZnO composite, the strong interaction is due to the condensation between the amino group of triazine and the surface hydroxyl groups of ZnO to form Zn-N bonds. Zn can also be implanted into the network of g-C₃N₄ by a post-annealing method by using Zn(NO₃)₂·6H₂O solution. The highly active g-C₃N₄-TiO₂ composite was fabricated by Yan *et al.*⁸¹ by mixing an appropriate amount of g-C₃N₄ and TiO₂ and by applying a simple impregnation method. Yin *et al.*⁸² synthesized SnO₂-g-C₃N₄ nanocomposites by an ultrasonic-assisted deposition method by using melamine and SnCl₄·5H₂O as the precursors at room temperature. It was found that the sphere-like SnO₂ nanoparticles with sizes of 2–3 nm were dispersed on the surface of g-C₃N₄ evenly in the SnO₂-g-C₃N₄ nanocomposites. SnO₂-g-C₃N₄ composite photocatalysts were synthesized by using SnCl₄·5H₂O solution in methanol by an ultrasonic-assisted deposition method at room temperature. Wang *et al.*⁸³ synthesized CeO₂-g-C₃N₄ nanocomposite by mixing CeO₂ with a suitable amount of g-C₃N₄ following a simple calcination technique. CeO₂ nanocrystals were synthesized by a solid-state decomposition reaction of (NH₄)₂CeO(NO₃)₆ at 500 °C, followed by mixing with different amounts of g-C₃N₄ in the solid state and then calcined to obtain the CeO₂-g-C₃N₄ composite. The CeO₂/g-C₃N₄ (13 wt%) composite represents the most optimal activity.

3.11. Synthesis of composites of g-C₃N₄ with narrow-bandgap transition metal species semiconductors

Many of the transition metal oxides can realize visible light photocatalysis due to their narrow bandgap. Some such transition metal oxides are discussed below.

By coupling N,S-TiO₂ with g-C₃N₄, the bandgap energy of TiO₂ decreases, making it visible light active and enhancing its light absorption ability and charge separation efficiency. Pany *et al.*⁸⁴ synthesized a N,S-TiO₂/g-C₃N₄ nanocomposite by using TiOSO₄·xH₂O and thiourea as precursor materials through a cost-effective thermal polymerization method. Fe₂O₃ was used by Hu *et al.*⁸⁵ to prepare an Fe³⁺-doped g-C₃N₄ composite photocatalyst, where the Fe³⁺ ions by coordinating to N-atoms were inserted at the interstitial position of g-C₃N₄. Chen *et al.*⁸⁶ prepared a mesoporous Fe-C₃N₄ nanocomposite by using SiO₂ nanoparticles as a hard template and dicyandiamide as the precursor to which FeCl₃ solution was added. Cheng *et al.*⁸⁷ recently reported a one-step method to incorporate FeOx into the g-C₃N₄ network by using ferrocene and urea as the starting materials. To improve the photocatalytic efficiency of g-C₃N₄, it was also coupled with a well-known p-type semiconducting

photocatalytic material Cu₂O, with a bandgap energy of 2.0–2.4 eV. The advantage of using Cu₂O is its low toxicity, low price and good environmental acceptability. Peng *et al.*⁸⁸ prepared a g-C₃N₄/Cu₂O composite by using Cu(CH₃COO)₂·H₂O solution by an alcohol-aqueous-based chemical precipitation method. In another method, a g-C₃N₄/Cu₂O composite was obtained by a hydrothermal method using a mixture of g-C₃N₄ and Cu(NO₃)₂. Zhou *et al.*⁸⁹ prepared a Cu(OH)₂/g-C₃N₄ composite by using mpg-C₃N₄, CuCl₂ and NaOH aqueous by a facile precipitation method. By the preparation of a Cu(OH)₂/g-C₃N₄ nanocomposite, the absorbed wavelength was estimated to be 470 nm, corresponding to a bandgap of 2.63 eV. He *et al.*⁹⁰ prepared a MoO₃-g-C₃N₄ composite from MoO₃ and melamine as the precursor by a direct mixing and calcination method; whereas Yuming *et al.*⁹¹ synthesized MoS₂/g-C₃N₄ heterojunction photocatalysts *via* a simple impregnation and heating method. A WO₃-g-C₃N₄ composite was prepared by Doan *et al.*⁹² by mixing crystalline WO₃ powder and melamine as the raw materials. WO₃ and melamine were mixed in 1 : 3 ratio and then subjected to calcination. The composite was then synthesized by the simple decomposition of melamine in the presence of WO₃ at 500 °C. When the sample was prepared by thermal treatment of the mixture at 500 °C, WO₃ was attached by a thin layer of g-C₃N₄ on the surface to form a g-C₃N₄-WO₃ composite. However, when the samples were treated at 600 °C and 700 °C, instead of the disappearance of g-C₃N₄, the presence of doping N in WO₃ was achieved. An In₂O₃-g-C₃N₄ hybrid was synthesized by Cao *et al.*⁹³ in a simple solvothermal method by mixing In(AO)₃ and g-C₃N₄ in the requisite proportions. In the In₂O₃-g-C₃N₄ hybrid, small In₂O₃ nanocrystals generated by the solvothermal process were uniformly distributed on the surface of g-C₃N₄. To develop different types of photocatalysts for water splitting, cobalt-based compounds play an important role. It has been reported that the coupling of spinel Co₃O₄, porous cobalt phosphate and cobalt hydroxide with g-C₃N₄ significantly enhances the water oxidation rate. Zhang *et al.*^{94,95} synthesized Co₃O₄-g-C₃N₄ from Co(NO₃)₂·6H₂O solution and neat g-C₃N₄ by an ultrasonication method while maintaining the pH. Among different transition metal oxides, NiO also acts as an efficient co-catalyst for photocatalytic water splitting. Zhang *et al.*⁹⁶ synthesized Ni- and NiO-loaded g-C₃N₄ by using Ni(NO₃)₂·6H₂O solution by a direct reduction method at 350 °C for 2 h or by oxidation in the presence of air at 200 °C for 1 h.

4. Anatomy of the structural and morphological characterizations of g-C₃N₄

Various research groups have worked a lot to optimize graphitic-C₃N₄ by structural, textural and morphological modifications. After the optimisation, different types of instrumental analysis, such as XRD, SEM, and TEM, were used to identify the crystal phase of the materials, the interlayer stacking, size of the nanoparticles and nature of the distribution of the nanoparticles in the composites. It was observed that in almost all the modified forms, g-C₃N₄ maintains its

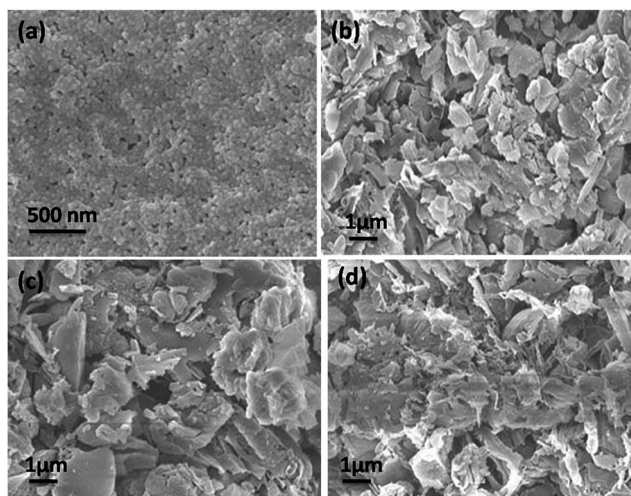


Fig. 7 SEM images of the $g\text{-C}_3\text{N}_4$ synthesized at different temperatures (a) 300 °C, (b) 400 °C, (c) 500 °C and (d) 600 °C (reproduced from ref. 22, licence number 3767470249553).

crystallinity and aromatic motif, showing the two typical characteristic peaks of the $g\text{-C}_3\text{N}_4$ polymer at 13.1° and at 27.4° in the XRD analysis. This indicates that the graphitic-like layered stacking of tri-*s*-triazine units in $g\text{-C}_3\text{N}_4$ is chemically robust towards textural modification. Zhang *et al.*²² reported that when the temperature increases gradually, $g\text{-C}_3\text{N}_4$ is gradually transformed into a crystalline or amorphous state as the degree of condensation depends on the starting material as well as on the temperature, which was confirmed by the slight broadening of the peaks. The morphology of the product also changes from spherical nanoparticles to layered $g\text{-C}_3\text{N}_4$ with an increase in temperature. The SEM and XRD analysis of the $g\text{-C}_3\text{N}_4$ obtained by the thermal polycondensation of melamine by varying the temperatures is shown in Fig. 7 and 8, respectively.

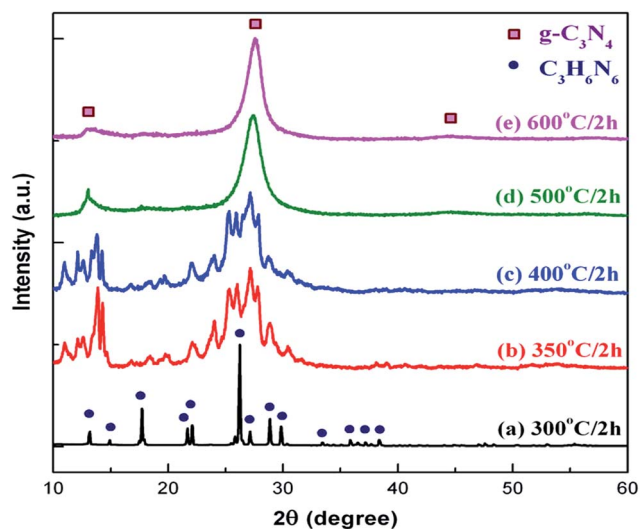


Fig. 8 XRD patterns of $g\text{-C}_3\text{N}_4$ synthesized at different temperatures for 2 h (reproduced from ref. 22, licence number 3767470249553).

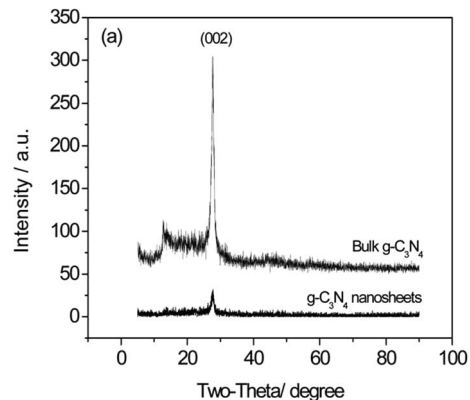


Fig. 9 XRD patterns of $g\text{-C}_3\text{N}_4$ nanosheets after exfoliation (reproduced from ref. 40, licence number 3767461234354).

In the case of a mesoporous structure, there is a gradual decrease of the peak intensity in the XRD analysis with increasing the condensation temperature because of the enlarged surface area and evident decrease in crystallinity due to the presence of mesopores in the polymeric structure. When there were texture changes, there was a considerable broadening of the XRD peaks, with a decreased intensity, thus indicating the size- and shape-dependent properties of the nanomaterials. According to Yang *et al.*,⁴⁰ after exfoliation, the intensity of the (002) peak in Fig. 9 is significantly decreased, clearly demonstrating the formation of $g\text{-C}_3\text{N}_4$ nanosheets.

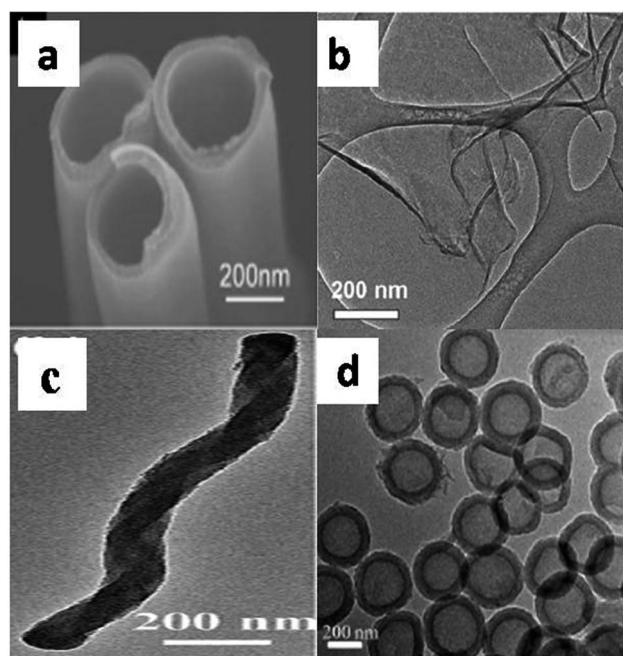


Fig. 10 TEM image of $g\text{-C}_3\text{N}_4$ nanotubes (a), nanosheets (b), nanorods (c) and hollow nanospheres (d) (reproduced with permission from ref. 20, Copyright American chemical society, 2009, ref. 40 (licence number 3767461234354), ref. 19 (licence number 3767470642681), ref. 44).

The surface morphology of different nanostructured $g\text{-C}_3\text{N}_4$ were characterized by SEM and TEM images. The surface study confirmed the nanoarchitecture and geometrical features of various textural modifications. The TEM image in Fig. 10 reveals the textural information about the nanoarchitecture of the material.

Modifications by different heteroatoms cause a narrowing of the bandgaps by lowering the HOMO levels. When the heteroatoms occupy the substitutional and interstitial positions, they alter their electronic properties to increase the efficiency. To modify the properties of $g\text{-C}_3\text{N}_4$ materials, non-metal doping has been extensively used. In F-, B- and P-modified $g\text{-C}_3\text{N}_4$ frameworks, the N-atom is substituted by the heteroatoms, resulting in a partial conversion of C-sp^2 to C-sp^3 . The incorporation of different amounts of doping reagents results in disturbance of the graphitic structure, which could be seen in the increased intensity of the (100) peak in the XRD analysis.

In I-doped $g\text{-C}_3\text{N}_4$, the sp^2 bonded N-atom is substituted by I atoms.⁵⁷ The electrons in I^{1-} were transferred into the carbon nitride network, and the iodine atom acted as the electron donor. The resultant I^+ and I^{7+} were stabilized by the available lone pair of electrons in the carbon nitride matrix. The π -conjugated system enhances the mobility of the photogenerated carriers by an interaction between iodine and $g\text{-C}_3\text{N}_4$. In the process of doping, the apparent colour of the CN-I_x sample changes with the increasing content of iodine from pale yellow to deep brown. In the CN-I_x sample, many micropores on the surface of the $g\text{-C}_3\text{N}_4$ layers were found, which resulted in an increased surface area. The surface area increased from $12 \text{ m}^2 \text{ g}^{-1}$ ($g\text{-C}_3\text{N}_4$) to $23 \text{ m}^2 \text{ g}^{-1}$ for $\text{I-g-C}_3\text{N}_4$.⁵⁸ In B- and F-co-doped materials, it was found that the B atoms enter C sites in the $g\text{-C}_3\text{N}_4$ network, while the F atoms saturate the residual bonds. The BN covalent bond also makes the material extremely stable. Boron- and fluorine-doped polymeric graphitic carbon nitride solid with a narrow pore size shows a spongy “morel-like” mesoporous structure of approximately 9.5 nm size, which shows its improved visible-light-induced photocatalytic activity.

Nanoparticles of noble metals, such as Ag, Au, Pt, Pd and Rh, can readily absorb visible light due to their surface plasmon resonance, which can be tuned by changing their size, shape and surrounding. The optical and electronic properties of metal nanoparticles, which are size and shape dependent, enhance the photocatalytic activity by promoting interfacial charge transfer in semiconductor–metal nanocomposites. The bandgap energy of the noble metal incorporated into the $g\text{-C}_3\text{N}_4$ nanoparticles can be lowered on the basis of surface plasmon effects^{62–75} and can show low photoluminescence intensity and excellent visible light absorption and superior photocurrent generation. When the photodeposition method is used as the loading process, Pt nanoparticles with an average diameter of 0.6 to 1.3 nm are obtained. However, when the impregnated method is used, the average diameter increases to 1.2 to 2.3 nm, with a uniform distribution of Pt nanoparticles on the surface. The oxidation state of Pt nanoparticles and the amount of the platinum species mainly depends on the different loading methods. The Pt nanoparticles are present on the surface of the catalyst in the form of Pt^{2+} or Pt^{4+} ions, which trap the

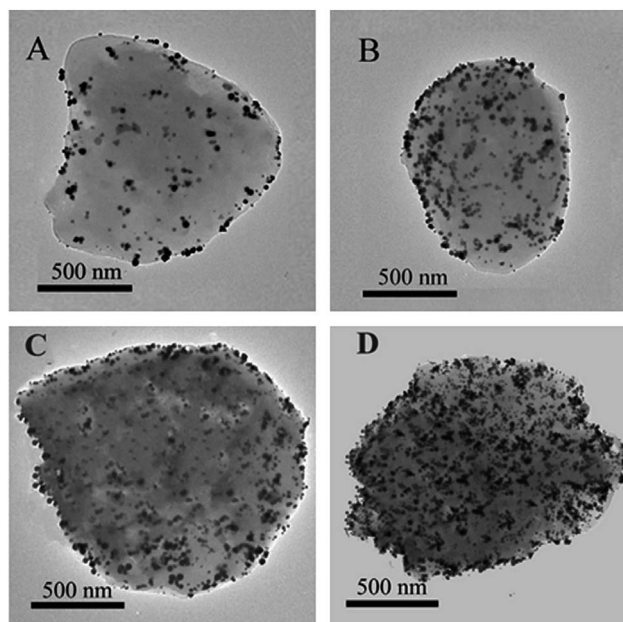


Fig. 11 TEM images of $\text{Au/g-C}_3\text{N}_4$ samples with different Au loading: (A–D) 20, 60, 80 and 90 wt% (reproduced from ref. 71, licence number 3767470882063).

photogenerated electrons to retard the recombination process; whereas in the $\text{Rh-g-C}_3\text{N}_4$ nanocomposite, the Rh NPs deposited on $g\text{-C}_3\text{N}_4$ surface are spherical and have approximately the same size as those of the neat one.⁶⁷ Between the Rh nanoparticles and the carbon nitride surface, a direct interaction exists.⁷⁰ In $\text{Au-g-C}_3\text{N}_4$, most of the Au NPs were dispersed in the range of 12–16 nm on the $g\text{-C}_3\text{N}_4$ support with different densities. The small Au NPs can be found on the layer of $g\text{-C}_3\text{N}_4$, which ultimately results in a composite photocatalyst. In the $\text{Au/g-C}_3\text{N}_4$ nanocomposite, $g\text{-C}_3\text{N}_4$ maintains a sheet-like layered structure consisting of graphitic planes stacked together with a conjugated aromatic system of triazine units. The Au NPs were found to be present linked to the surface and

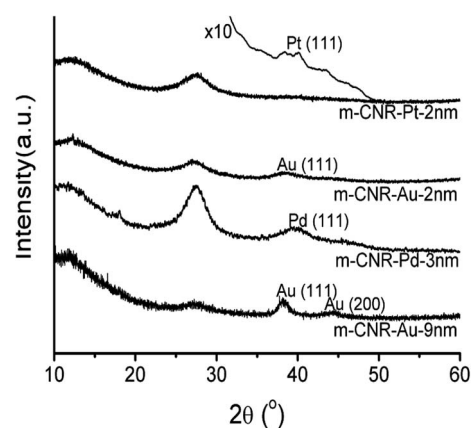


Fig. 12 XRD patterns of m-CNR (mesoporous carbon nitride)-supported noble metal NPs, (reproduced from ref. 73).

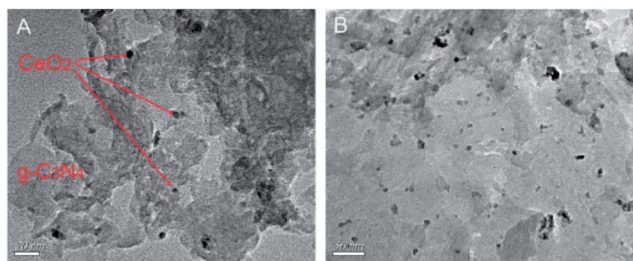


Fig. 13 TEM images of (A) $\text{CeO}_2/\text{g-C}_3\text{N}_4$ (5.9%) composite and (B) $\text{CeO}_2/\text{g-C}_3\text{N}_4$ (13.0%) composite (reproduced from ref. 83).

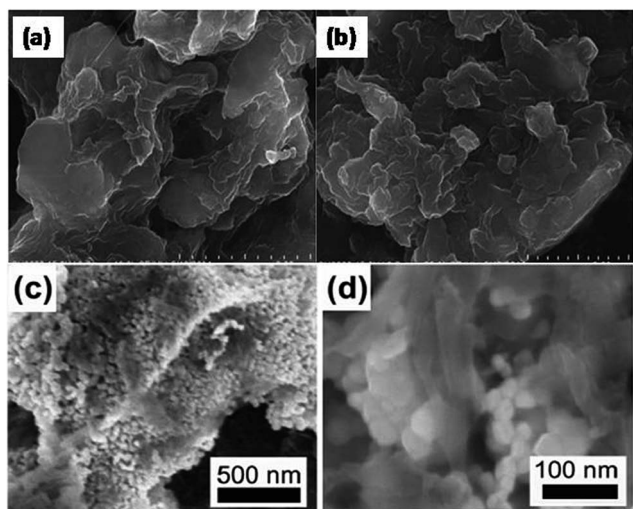


Fig. 14 SEM images of: (a) $\text{g-C}_3\text{N}_4$, (b) $\text{g-C}_3\text{N}_4\text{-FeO}$ composite (c) $\text{g-C}_3\text{N}_4\text{-ZnO}$ (8.4), and (d) $\text{g-C}_3\text{N}_4\text{-ZnO}$ (15.6) (reproduced from ref. 80 and 85).

edges of the $\text{g-C}_3\text{N}_4$ sheet. TEM images of $\text{Au/g-C}_3\text{N}_4$ samples with different Au loading are presented in Fig. 11.

Li *et al.*⁷³ reported that the XRD patterns of Au-, Pt- and Pd-co-doped $\text{g-C}_3\text{N}_4$ show the same reflections as for mesoporous $\text{g-C}_3\text{N}_4$ along with the characteristic peaks for the noble metals, as shown in the Fig. 12.

Transition metal ion or oxide nanoparticles were incorporated into $\text{g-C}_3\text{N}_4$, and the XRD patterns remained almost unchanged, typically showing two diffraction peaks corresponding to the 002 and 100 planes, thus maintaining the same crystallinity in the composite. In few cases, a slightly shifted peak from 27.4° towards a higher angle represented a certain decrease in the interplanar stacking distance. The interaction between the transition metal ions or oxides nanoparticles and $\text{g-C}_3\text{N}_4$ are strong and were dispersed evenly on the surface of $\text{g-C}_3\text{N}_4$. Wang *et al.*⁸³ reported that in $\text{CeO}_2/\text{g-C}_3\text{N}_4$ (13 wt%), CeO_2 nanoparticles with diameters of about 5–20 nm are attached to the surface and to the edge of the $\text{g-C}_3\text{N}_4$. The agglomeration of CeO_2 particles can be observed with an increase in the CeO_2 wt% in the $\text{CeO}_2\text{-g-C}_3\text{N}_4$ nanocomposite. The interaction between the CeO_2 nanoparticles and the $\text{g-C}_3\text{N}_4$ layered materials was so strong that even after a long ultrasonication treatment at room temperature, the composite could not be destroyed. Fig. 13 shows the TEM images of the $\text{CeO}_2/\text{g-C}_3\text{N}_4$ samples, showing the formation of the composite.

The morphologies and the particle sizes of the synthesized composites were studied by SEM (Fig. 14). In the case of neat $\text{g-C}_3\text{N}_4$, a large number of irregular particles were found because of the evolution of gases during the calcinations. However, the SEM images of the composites reveal that the nanocrystals were well spread out over the surface of $\text{g-C}_3\text{N}_4$. However, over-coverage of the nanocrystals may reduce the number of reactive sites on the surface of $\text{g-C}_3\text{N}_4$, thus resulting in a decreased photocatalytic activity.

5. Study of the optical and electronic properties of $\text{g-C}_3\text{N}_4$ -based materials

The main purpose of the modification of $\text{g-C}_3\text{N}_4$ is to modulate its electronic and optical properties. Bandgap narrowing can be effectively used to modify the absorption edge of a semiconductor photocatalyst to extend its absorption in the visible region. The modulation of $\text{g-C}_3\text{N}_4$ by doping with non-metals or by the formation of composites with other narrow-bandgap photocatalysts could effectively enhance the light absorption

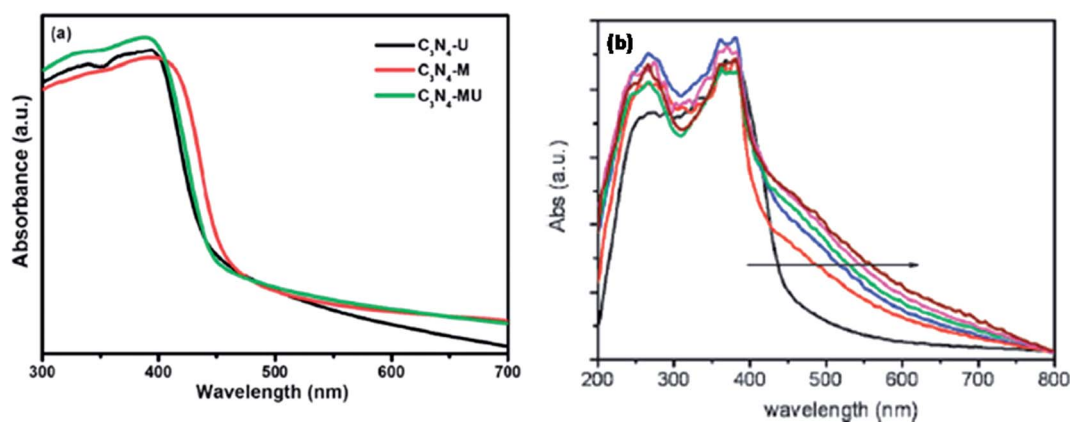


Fig. 15 (a) UV-Vis DRS of neat $\text{g-C}_3\text{N}_4$ and (b) mesoporous $\text{g-C}_3\text{N}_4$ prepared by using different amounts of P123 (reproduced from ref. 3 and 30).

property of $g\text{-C}_3\text{N}_4$ in the wide range of the visible region, which was confirmed by UV-Vis DRS. Many researchers have reported that morphological changes and the inclusion of various metal-ion species in the $g\text{-C}_3\text{N}_4$ network alter its bandgap energy and enhance its light absorption significantly.

An insight into the optical property of $g\text{-C}_3\text{N}_4$ indicates that neat $g\text{-C}_3\text{N}_4$ shows absorption up to 450 nm, which then changes significantly by morphological variation. Yan *et al.*³⁰ reported a remarkable red-shift in optical absorption from 450 nm to 800 nm by synthesising mesoporous $g\text{-C}_3\text{N}_4$ using the P123 surfactant. The following figures (Fig. 15a and b) show the UV-Vis DRS of neat $g\text{-C}_3\text{N}_4$ prepared from various precursors and mesoporous $g\text{-C}_3\text{N}_4$ prepared with different amounts of P123, in which the arrow indicates the increasing amount of P123.

By preparing ompg- C_3N_4 , the surface area increased to $239\text{ m}^2\text{ g}^{-1}$ and it exhibited better optical absorption than bulk $g\text{-C}_3\text{N}_4$, especially in the 430–550 nm region. According to Yang *et al.*,⁴⁰ after exfoliation, the surface area of the material was as high as $384\text{ m}^2\text{ g}^{-1}$ and it contained an ample number of nitrogen-containing active sites, which are favourable to enhance its photocatalytic activity. Bai *et al.*⁴⁵ reported that while preparing hollow carbon nitride nanospheres, with the increase in the amount of added organic compound, the sample showed a red-shift from 420 nm to 700 nm.

Photoluminescence is another useful technique to study the migration, transfer and separation efficiency of semiconducting materials. The separation of charge carriers in $g\text{-C}_3\text{N}_4$ can be effectively minimized by doping with cations, by loading of noble metals or by the formation of composites with other metal oxides *etc.* to improve its photocatalytic efficiency towards hydrogen production. Martha *et al.*³ reported the synthesis of a highly active $g\text{-C}_3\text{N}_4$ photocatalyst from a mixture of urea and melamine, which showed a reduced electron-hole recombination rate and enhanced photocatalytic activity, as shown in Fig. 16.

Heteroatoms such as N, C, B, F, S, and P are most commonly used to shift the optical absorption in the visible

region by creating localized/delocalized states in the bandgap, providing improved activities in the samples for photocatalytic hydrogen production. Non-metal doping decreases the energy gap to enhance the visible light absorption of $g\text{-C}_3\text{N}_4$, which is at a maximum when the doping occurs in the interstitial sites and is due to a significant change in the distribution pattern of the $g\text{-C}_3\text{N}_4$ sheets. The bandgap of CNF decreases from 2.69 eV for $g\text{-C}_3\text{N}_4$ to 2.63 eV by⁴⁷ fluorine doping. With the decrease in bandgap energy, the semiconductor properties of the F-doped $g\text{-C}_3\text{N}_4$ have slightly been changed, with a shift of the absorption in the visible region. Similarly B-doped $g\text{-C}_3\text{N}_4$ also shows a slightly reduced bandgap of 2.66 eV as compared to pure $g\text{-C}_3\text{N}_4$ (2.7 eV).⁴⁹ In the case of⁵² P-doped $g\text{-C}_3\text{N}_4$, it was also found that with the increasing P percentage, the optical bandgap energy gradually changes to lower energy. Compared to undoped $g\text{-C}_3\text{N}_4$, the P-doped $g\text{-C}_3\text{N}_4$ showed a significantly enhanced electrical conductivity by up to 4 orders of magnitude. It was also found that the photocurrent generation was increased 5-fold. Both of these are important steps towards the photovoltaic application of $g\text{-C}_3\text{N}_4$. When the percentage of P-atoms is moderate, the bandgap changes in such a manner that, UV-Vis absorption indicates the presence of some intermediate states between VB and CB. In the case of C- $g\text{-C}_3\text{N}_4$, the bandgap energy value was found to be 2.56 eV.⁵³ As photoexcitation strongly depends on the bandgap of the semiconductor and the wavelength of the light used, C- $g\text{-C}_3\text{N}_4$ should absorb more visible light than $g\text{-C}_3\text{N}_4$. In S-doped $g\text{-C}_3\text{N}_4$, it was found that the nitrogen atoms of the melon ring were replaced by sulphur atoms, resulting in a unique electronic structure.⁵⁵ There was an increase in the bandgap, which showed a slightly decreased absorbance in the visible region. The bandgap of $g\text{-C}_3\text{N}_4\text{-}x\text{S}_x$ was shifted from 2.73 eV to 2.85 eV.⁵⁶ The most interesting synergistic phenomenon of sulphur involved a widening and upshifting of the VB, which was achieved through the homogenous distribution of the S dopant and a reduction in particle size after doping. Enhanced light harvesting was evidenced from the UV-Vis diffuse reflectance spectra (DRS) by the upshift of the absorbance of S- $g\text{-C}_3\text{N}_4$ compared to porous and non-porous $g\text{-C}_3\text{N}_4$ samples. For mpg-CNS, the bandgap energy decreases to 2.61 eV, which

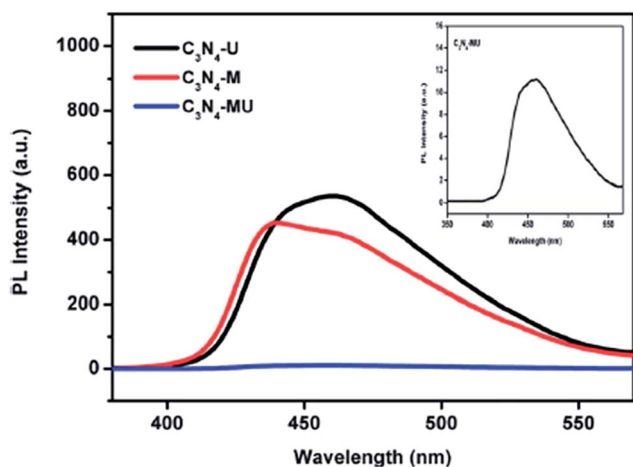


Fig. 16 PL spectra of $g\text{-C}_3\text{N}_4$ prepared from a mixture of urea and melamine (reproduced from ref. 3).

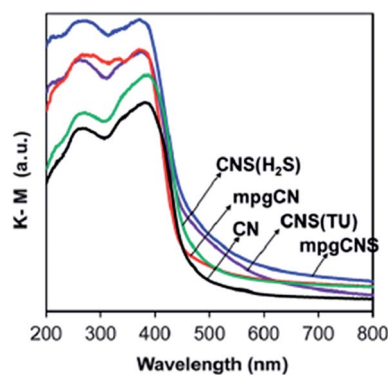


Fig. 17 UV-Vis DRS of mpg-CNS and mpg-CN (reproduced from ref. 56).

results in a downshift of the conducting band, as shown in Fig. 17.

The absorption band edge extends from 420 nm to 600 nm in⁵⁷ I-doped g-C₃N₄ causing a red-shift. The red-shift is due to the effective extension of the aromatic carbon nitride heterocycle by iodide ions and due to the presence of iodine atoms as an impurity in the energy levels above the valence band edge. The band gap energy decreased from 2.75 eV to 2.69 eV (~0.06 eV). The self-doping strategy of g-C₃N₄ tunes the surface property, electronic structure and, hence, its photoreactivity. In carbon self-doped g-C₃N₄, it was found that the bridging N-atoms are substituted by the C-atoms. This increases the delocalized π -bonds between the substituted carbons, which increases the electrical conductivity of g-C₃N₄ as delocalized π -bonds favour the electron transfer. The bandgap of g-C₃N₄ decreases with carbon self-doping and enhances its visible light absorption and photocatalytic performance. According to Dong *et al.*, when preparing C-g-C₃N₄, the particle size decreases in comparison to g-C₃N₄. Therefore, carbon self-doping induces electrical conductivity increases due to the reduction in particle size. The photocurrent generation of C-g-C₃N₄ is 1.39 times higher than that of g-C₃N₄. Besides this post-treatment doping, when sulphur is doped into the g-C₃N₄ matrix by the polycondensation of sulphur-enriched trithiocyanic acid, -SH groups present at the terminal of the melon ring are the leading group. The absorption in the visible region increases due to the presence of residual S in the resulting S-doped g-C₃N₄ as compared to undoped g-C₃N₄.

Nanoparticles of noble metals, such as Ag, Au, Pt, Pd, Rh, can strongly absorb visible light due to their surface plasmon resonance, which can be tuned by changing their size, shape and surroundings. The optical and electronic properties of metal nanoparticles that are size and shape dependent, enhances the photocatalytic activity by promoting interfacial charge transfer in semiconductor-metal nanocomposites. The bandgap energy of the noble metal nanoparticles can be lowered on the basis of the surface plasmon effects and show low photoluminescence intensity and excellent visible light absorption as well as superior photocurrent generation. In Pt-g-C₃N₄ nanospheres (NS-g-C₃N₄), the surface area increases to 160 m² g⁻¹ and the pore volume was found to be 0.4 cm³ g⁻¹. NS-g-C₃N₄ shows a hypsochromic shift of the absorption edge from 465 nm to 430 nm and a bandgap energy increase from 2.67 eV to 2.86 eV. Due to the multiple reflections of the sharp edges in the defect sites, the absorption region extends from 430 nm to 590 nm. The 3D interconnected nanosheets shorten the distance for charge migration and help the electron delocalization.⁷⁰⁻⁷⁴ Au and Ag nanoparticles show good photocatalytic performances by lowering the bandgap energy due to the surface plasmon effects. The photocatalytic activity of g-C₃N₄ can be improved by coupling it with simple silver salts, like Ag₃PO₄, or by preparing Ag/AgCl/g-C₃N₄ composites or Ag/AgBr/g-C₃N₄ nanocomposites. Zhang *et al.*⁵⁹ reported that silver orthophosphate (Ag₃PO₄) is a novel silver salt that shows an extremely high quantum yield of about 80% at wavelengths less than 480 nm for O₂ evolution. When Ag₃PO₄ is coupled with highly stable metal-free polymeric g-C₃N₄, the photocatalytic

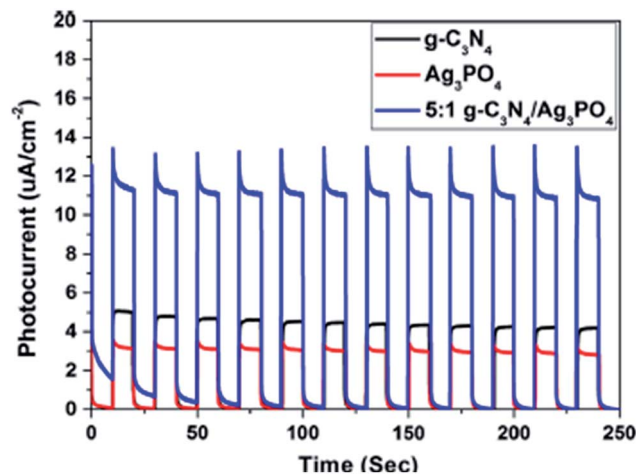


Fig. 18 Photocurrent density of 5 : 1 g-C₃N₄/Ag₃PO₄ bulk heterojunction (reproduced from ref. 59).

activity of both g-C₃N₄ and Ag₃PO₄ increases. The insoluble g-C₃N₄ protects Ag₃PO₄ from dissolution and enhances its stability. The CB and VB potentials of g-C₃N₄ are more negative than that of Ag₃PO₄, which enhances the charge transfer separation process through their interface. The efficient charge separation process was further confirmed by photocurrent measurements (Fig. 18). The pure g-C₃N₄ and Ag₃PO₄ exhibited a photocurrent density of 4.7 and 3.1 $\mu\text{A cm}^{-2}$, respectively. However, due to the synergistic effect between g-C₃N₄ and Ag₃PO₄, 5 : 1 g-C₃N₄/Ag₃PO₄ bulk heterojunction showed a photocurrent density of 11.2 $\mu\text{A cm}^{-2}$, which was even more than the sum of the photocurrent density of pure g-C₃N₄ and pure Ag₃PO₄.

As a direct semiconductor, a narrow bandgap of Ag₂S (1.1 eV) increases its absorption and extends its application in photovoltaic cells and photocatalytic applications. Au nanoparticles show good absorption in visible light due to the surface plasmon resonance, which is necessary for the enhancement of photocatalytic activity, causing a red-shift compared to that of neat g-C₃N₄. The bandgap energies also change from 2.71 eV for neat g-C₃N₄ to 2.63 eV in the case of Au/g-C₃N₄. This reduction in bandgap energy of 1 wt% Au/g-C₃N₄ is due to the plasmonic effect of AuNPs, resulting in an enhancement of photocatalytic H₂ production. The incorporation of AuNPs onto the layer of g-C₃N₄ restricts recombination between the opposite charge carriers and enhances the photocatalytic activity. It was observed that with the deposition of AuNPs onto g-C₃N₄, the current density was significantly increased. 1 wt% Au/g-C₃N₄ produced a photocurrent density of 49.5 mA cm⁻², whereas in neat g-C₃N₄, it was only 15 $\mu\text{A cm}^{-2}$, which is more than 3000 times higher, which was simply due to the enhanced visible light absorption. Also the enhancement of photocatalytic activity of the nanocomposite photocatalysts can be explained on the basis of their PL spectra, which further confirm the migration of photo-generated charge carriers and the delayed recombination process. As compared to neat g-C₃N₄, the decreased PL

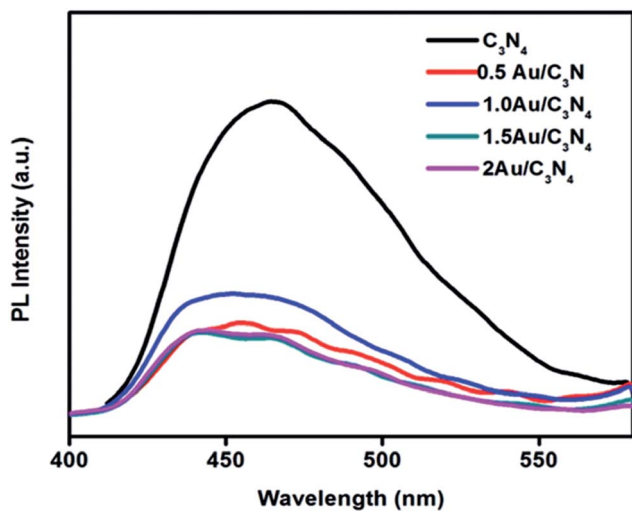


Fig. 19 PL spectra of neat $g\text{-C}_3\text{N}_4$ and $\text{Au}/g\text{-C}_3\text{N}_4$ nanocomposites (reproduced from ref. 70).

intensity of all the $\text{Au}/g\text{-C}_3\text{N}_4$ nanocomposites in Fig. 19 indicates the improved electron–hole separation.

Chang *et al.*⁷⁵ reported that $\text{Pd}/\text{mpg-C}_3\text{N}_4$ shows a significant increase in light absorption in the visible region. On increasing the Pd content, the colour of the catalysts changed from yellowish to light grey, and their light absorbance increased gradually from 200 nm to 700 nm. When the Pd content was more than 1.5%, the absorbance even shifted to the near infrared. $\text{Pd}/\text{mpg-C}_3\text{N}_4$ with 4.50% Pd is the optimum loading and shows a wide absorbance in the UV-Vis region. In $\text{Pd}/\text{mpg-C}_3\text{N}_4$, Pd is present as Pd^0 and acts as an electron trapping agent, and the separation of photogenerated electrons and holes increases, and consequently the photocatalytic performance is improved.

The electronic and optical functions of $g\text{-C}_3\text{N}_4$ can be easily modified after transition metal-ion doping. The transition metal species, by lowering the bandgap, extends the light absorption into the visible region of the electromagnetic spectrum. In determining electrical conductivity in a material, the bandgap is a major factor and it directly determines the upper wavelength limit of light absorption, and hence affects the photocatalytic activity. Tetragonal tin dioxide (SnO_2) is a multifunctional material has been widely used in the fields of solar cells, gas sensing, photovoltaic conversion and photocatalysis. However, the bandgap of SnO_2 is so wide (3.7 eV) that it can absorb only UV light for the degradation of pollutants in water and air. However, SnO_2 is a better electron acceptor than TiO_2 and ZnO . So by preparing a $\text{SnO}_2\text{-}g\text{-C}_3\text{N}_4$ composite, the electron–hole separation tendency of $g\text{-C}_3\text{N}_4$ can be increased and hence so can its photocatalytic activity. The rare earth oxide CeO_2 finds application as a photoactive material in solar cells and also as a photocatalyst in the degradation of organic pollutants, as well as in the production of hydrogen.⁸³ But it mainly absorbs in the near UV region. However, when it is coupled with $g\text{-C}_3\text{N}_4$, the $\text{CeO}_2\text{-}g\text{-C}_3\text{N}_4$ composite has an extended application as a photocatalyst in the visible region. In

another example, the absorption wavelength of TiO_2 nanofibres was under 400 nm, but after coupling $g\text{-C}_3\text{N}_4$ with TiO_2 nanofibres, the hybrid showed more efficient light absorption from 400 nm to 800 nm in comparison with the pure $g\text{-C}_3\text{N}_4$ and TiO_2 .⁸¹ Although, the surface area of the $g\text{-C}_3\text{N}_4\text{-TiO}_2$ composite is less, the notable increase in the photocatalytic activity might be related with the participation of $g\text{-C}_3\text{N}_4$ in the charge separation process. Thus, a higher efficiency in the electronic step leads to higher photocatalytic activity, with an improvement up to 70%. Similarly, the absorption edge of TiO_2 corresponds to a bandgap of 3.2 eV, which is in the UV region. However, according to Pany *et al.* in $\text{N,S-TiO}_2/g\text{-C}_3\text{N}_4$ nanocomposites, compared to TiO_2 , the absorption edge is shifted towards the shorter wavelength region, making it visible light active. Moreover, in $\text{N,S-TiO}_2/g\text{-C}_3\text{N}_4$ photocatalysts, the gradual increase in wt% of thiourea plays a key role in the absorption shift towards the red end with respect to Ti. Cu_2O is a well-known p-type semiconducting photocatalytic material with a bandgap energy of 2.0–2.4 eV. To improve the photocatalytic efficiency of $g\text{-C}_3\text{N}_4$, it was also coupled with Cu_2O . Peng *et al.*⁸⁸ reported that when Cu_2O was coupled with $g\text{-C}_3\text{N}_4$, it exhibited enhanced photocatalytic activity, because of the well-matched overlapping band structures and resulting highly efficient separation of photogenerated charges. Pure $g\text{-C}_3\text{N}_4$ possesses an absorption wavelength of ~ 450 nm, whereas Cu_2O possess a broad absorption in the visible region from 400 to 600 nm. So after combining these two semiconductors, the absorption of $g\text{-C}_3\text{N}_4\text{-Cu}_2\text{O}$ in the visible light range remarkably increases. Also, the absorption intensity of $g\text{-C}_3\text{N}_4\text{-Cu}_2\text{O}$ increases with the increase in Cu_2O content. It was found that when⁹³ In_2O_3 and $g\text{-C}_3\text{N}_4$ with appropriate band alignments were coupled, there was an interfacial charge transfer, which increases the separation efficiency of the photogenerated electrons and holes. The well-dispersed In_2O_3 nanocrystals on sheet-like $g\text{-C}_3\text{N}_4$ surfaces form an intimate interaction. Since the conduction band (CB) and the valence band (VB) positions of In_2O_3 lie at ~ -0.6 eV and $+2.2$ eV, respectively, and as both are lower than those of $g\text{-C}_3\text{N}_4$, *i.e.* ~ -1.1 eV and $+1.6$ eV, respectively, this allows effective interfacial charge transfer across the In_2O_3 and $g\text{-C}_3\text{N}_4$ hybrid.

6. Photocatalytic hydrogen production

After the breakthrough report by Fujishima and Honda in 1972, research has been going on to develop photocatalysts with high efficiency and stability for water splitting to produce hydrogen gas. Studies by different groups of scientists have found that neat $g\text{-C}_3\text{N}_4$ can undergo two cycles of water splitting under visible light successfully. The semiconductor photocatalyst $g\text{-C}_3\text{N}_4$ is considered to be suitable for water splitting as it has a bandgap value greater than 1.23 eV (redox potential of water) and also proper positioning of the CB and VB levels. For water splitting, the bottom level of the conduction band of the semiconductor has to be more negative than the redox potential of H^+/H_2 (0 V vs. the normal hydrogen electrode (NHE)), whereas the valence band of the semiconductor has to be more positive

than the redox potential of O₂/H₂O (1.23 eV). One half of the reaction is a water-reduction half-cycle, which produces H₂, and the other half is a water-oxidation half-cycle to form O₂. Although the band potentials are appropriate, g-C₃N₄'s photocatalytic efficiency is still low due to the fast recombination of charge carriers and the mismatch between its bandgap and solar spectra. Because of this, the material has been optimized by morphological and textural variation, non-metal doping, noble metal incorporation and transition metal- and metal oxide modification. In this review, we have tried to summarize the key modifications of g-C₃N₄ to increase the quantum yield. Doping and various modifications are expected to increase the carrier mobility, while the non-coplanar HOMO and LUMO improve the separation of photogenerated e⁻/h⁺ pairs to enhance the photocatalytic activity.

6.1. Hydrogen production by neat g-C₃N₄

For the first time, Wang *et al.* predicted that g-C₃N₄ is thermodynamically stable under light irradiation and is capable of water splitting in the presence of a sacrificial agent. The proper bandgap of g-C₃N₄ in particular makes it suitable for applications in photochemistry and photocatalysis. g-C₃N₄ can be prepared from different precursors (550 °C, 5 °C min⁻¹ ramp rate), and when tested for HER in an aqueous sacrificial solution containing triethanolamine (TEOA) at room temperature and atmospheric pressure, it was found that urea-derived g-C₃N₄ exhibited the highest H₂ evolution in comparison to DCDA

or thiourea-derived g-C₃N₄ under visible light irradiation. The HER of urea-derived g-C₃N₄ is 20 000 μmol h⁻¹ g⁻¹, which is 15 times more than that of DCDA-derived g-C₃N₄ and 8 times more than that of thiourea-derived g-C₃N₄. However, the g-C₃N₄ obtained from dicyanamide exhibits the highest activity.⁴

g-C₃N₄ is a better semiconductor photocatalyst than the other developed traditional photocatalysts owing to its stability, visible light absorption property and appropriate band edge potentials for water splitting reactions. Herein, we have briefly presented a comparative study of various class of photocatalysts, including oxides, sulphides, nitrides, oxynitrides, *etc.*, which have been widely used for H₂ production. The details regarding materials, the light source, reaction solution and H₂ evolution are presented in Table 2.

g-C₃N₄ is further modified in various ways for enhancement of its H₂ production ability. Groenewolt *et al.*³⁸ reported the preparation of mpg-C₃N₄ nanoparticles, where the particle size of g-C₃N₄ could be easily replicated, ranging from 5 to 7 nm, by using a mesoporous silica template, and managed to increase the specific surface area to 400 m² g⁻¹, which would result in the photocatalytic H₂ evolution being enhanced nearly 10-fold.

According to Yang *et al.*,⁴⁰ after exfoliation, the photocatalytic HER of g-C₃N₄ nanosheets was evaluated from water/triethanolamine mixtures in visible light and with Pt (3 wt%) as the co-catalyst, and it was found to be 93 μmol h⁻¹, which is much higher than the value for bulk g-C₃N₄, which is 10 μmol h⁻¹.

Zheng *et al.*^{42,43,45} extensively studied the photocatalytic H₂ evolution of hollow carbon nitride nanospheres (HCNS) and

Table 2 Comparative study of various classes of photocatalysts towards photocatalytic hydrogen production

| Photocatalyst | Incident light (λ) | Reaction solution | H ₂ evolution (μmol h ⁻¹ g ⁻¹) | Reference |
|--|--------------------|---|--|-------------|
| TiO ₂ | 250–400 nm | CH ₃ OH | Pt/~3300 | 97 |
| TiO ₂ nanosheets | 250–400 nm | CH ₃ OH | 117.6 | 98 |
| ZnO | ≥420 nm | Na ₂ S | 44 000 | 99 |
| CeO ₂ | ≥300 nm | Ce ⁴⁺ | — | 100 |
| LaTiO ₃ | 250–400 nm | Pure water | NiO _x /137 | 101 |
| SrTiO ₃ | 250–400 nm | NaOH | NiO _x /~70 | 102 |
| NaTiO ₃ : La | 250–400 nm | Pure water | NiO/19 800 | 103 and 104 |
| PbWO ₄ | 290–600 nm | Pure water | RuO ₂ /96 | 105 and 106 |
| BiVO ₄ | ≥420 nm | AgNO ₃ | — | 107 |
| CdS | ≥420 nm | Na ₂ S + Na ₂ SO ₃ | Pt/27 333 | 108–110 |
| In ₂ S ₃ | ≥400 nm | Na ₂ S + Na ₂ SO ₃ | Pd/960.2 | 111 |
| ZnIn ₂ S ₄ | ≥420 nm | Na ₂ S + Na ₂ SO ₃ | Pt/231 | 112 |
| AgGaS ₂ | ≥420 nm | Na ₂ S + Na ₂ SO ₃ | Pt/2960 | 113 |
| CuGa ₃ S ₂ | ≥420 nm | Na ₂ S + Na ₂ SO ₃ | NiS/~2800 | 114 |
| ZnS | ≥420 nm | Na ₂ S + Na ₂ SO ₃ | 232.7 | 115 |
| Cd In ₂ S ₄ | ≥420 nm | H ₂ S + KOH | 6960 | 116 |
| CuInS ₂ | ≥420 nm | Na ₂ S + Na ₂ SO ₃ | Pt/84 | 117 |
| TiN | ≥400 nm | Na ₂ S | Pt/150 | 118 |
| Ta ₃ N ₅ | ≥420 nm | CH ₃ OH/AgNO ₃ | Pt/~125 | 119 |
| Ge ₃ N ₄ | ≥200 nm | H ₂ SO ₄ | RuO ₂ /3600 | 120 |
| GaN | ≥300 nm | H ₂ SO ₄ | Rh _{2-x} Cr _x O ₃ /63.3 | 121 |
| TaON | ≥420 nm | C ₂ H ₅ OH/AgNO ₃ | Ru/300 | 122 |
| La TiO ₂ N | ≥420 nm | CH ₃ OH/AgNO ₃ | Pt/~15 | 123 |
| Y ₂ Ta ₂ O ₅ N ₂ | ≥420 nm | C ₂ H ₅ OH/AgNO ₃ | Pt–Ru/833 | 124 |
| Zr ₂ ON ₂ | ≥420 nm | CH ₃ OH/AgNO ₃ | Pt/7 | 125 |
| Ga–Zn-in mixed oxy nitride | ≥400 nm | CH ₃ OH/AgNO ₃ | Rh/50 | 126 |
| TaO _x N _y | ≥400 nm | CH ₃ OH | 3.12 mmol g ⁻¹ h ⁻¹ | 127 |
| Zn–Ga–Ge–N–O | ≥400 nm | H ₂ C ₂ O ₄ | (~62 μmol h ⁻¹) | 128 |

Table 3 Comparative study of H₂ evolution by morphological variation of g-C₃N₄ using Pt as a co-catalyst

| Texture | Morphology | Surface area (m ² g ⁻¹) | Incident light (λ) | Reaction solution | H ₂ evolution (μmol h ⁻¹) | Reference |
|---|--------------------------------|--|--------------------|-------------------|--|-----------|
| Bulk g-C ₃ N ₄ | Nanopowder | 13.4 | ≥420 nm | Triethanolamine | 12.5 | 18 |
| g-C ₃ N ₄ | Nanosheets | 84.2 | ≥420 nm | Methanol | 93 | 40 |
| | Structure-distorted nanosheets | 99 | ≥420 nm | Triethanolamine | 177 | 42 |
| | Hollow nanospheres | 221 | ≥420 nm | Triethanolamine | 275 | 44 |
| mpg-C ₃ N ₄ using silica nanoparticles | | 400 | ≥420 nm | Triethanolamine | 125 | 38 |
| mpg-C ₃ N ₄ using soft template (10 wt% P123) | | 90 | ≥420 nm | Triethanolamine | 148.2 | 30 |
| ompg-C ₃ N ₄ | o-Cylindrical pores | 142 | ≥420 nm | Triethanolamine | 26.5 | 31 |

found that the H₂ evolution was increases 3-fold (278 μmol h⁻¹) by using Pt (3 wt%) as a co-catalyst. Also, by changing the condensation temperature, the photocatalytic H₂ evolution varies. The HCNS-550 °C exhibited a HER of 275 μmol h⁻¹, which is about 2 times higher than that of HCNS. The HER of HCNS-300 °C was found to be 202 μmol h⁻¹, which is much higher than the HCNS-400 °C and HCNS-500 °C samples. The comparative study of H₂ evolution rates are presented in Table 3.

6.2. Hydrogen production by non-metal-doped g-C₃N₄

Wang *et al.*⁴⁷ studied the photocatalytic activity of F-doped g-C₃N₄ towards HER from water under visible light (λ > 420) and in the presence of Pt (3 wt%) as a co-catalyst, as shown in Fig. 20, and found that CNF_x samples (x = 0.5 g) showed higher H₂ evolution activity over g-C₃N₄, which was about 2.7 times more than that of neat polymeric g-C₃N₄. These catalysts are highly stable and can be easily separated from the reaction solution by simple filtration. Furthermore, they can be reused for several cycles without losing activity. Hence, the CNF samples provide a modified texture with a decreased optical bandgap and improved activities for the photocatalytic hydrogen production from water/TEA.

The HER of C-g-C₃N₄ was 1.42 times greater than that of neat g-C₃N₄. Carbon self-doped g-C₃N₄ synthesised by Zhang *et al.* by the copolymerization of dicyandiamide with barbituric acid

increased the HER by nearly 4-fold that of neat g-C₃N₄. All these enhanced photocatalytic activities were due to the separation and transfer of photoinduced charge carriers. The polymeric CNS sample undergoes the water oxidation reaction without the need for the addition of co-catalysts, which is not possible for the undoped g-C₃N₄. Similarly, S-doped g-C₃N₄, due to its unique electronic structure, had a special photocatalytic activity towards HER, which was 8 times⁵⁴ higher than that of neat g-C₃N₄ under visible light. However, according to Hong *et al.*,⁵⁶ by doping a small percentage of S in mesoporous g-C₃N₄, the photocatalytic HER was remarkably improved. The HER of mpg-CNS was about 136 μmol h⁻¹, which was 214% higher than that of CNS and 36% higher than that of the mpg-CN samples. Due to both the mesoporous structure and sulphur doping, the activity of mpg-CNS towards hydrogen evolution from photocatalytic water splitting was enhanced almost 30-fold⁵⁶ compared to that of pure g-C₃N₄, although the surface increase was only 10-fold, as shown in Fig. 21. The quantum efficiency was found to be as high as 5.8% at 440 nm in an aqueous solution of triethanolamine. But *ex situ* sulphur doping was found to be less effective towards photocatalytic performance.

Zhang *et al.*⁵⁷ reported that iodine modification is considered to be a good dopant to enhance the photocatalytic performance based on the optical characterization and hydrogen evolution activity. Also, the photocatalytic activities of halide-ions-doped g-C₃N₄ were greater in comparison to pure g-C₃N₄. An I-g-C₃N₄ sample showed the fastest HER (about 38 μmol h⁻¹),

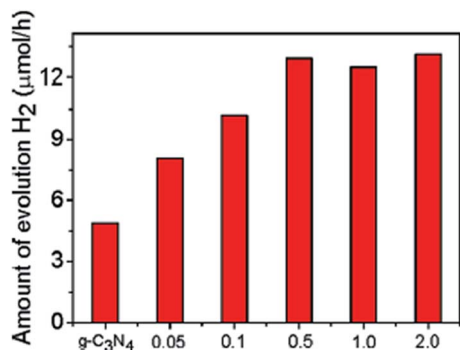


Fig. 20 Photocatalytic activity of F-doped g-C₃N₄ towards HER from water/TEA under visible light (λ > 420) (reproduced from ref. 47, licence number 3767471256893).

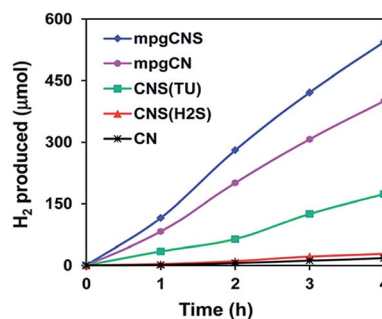


Fig. 21 Hydrogen evolution of S-doped g-C₃N₄ from an aqueous solution of TEA under visible light (λ > 400) (reproduced from ref. 56, licence number 3767480308846).

Table 4 Comparative study of the hydrogen evolution rates of the g-C₃N₄ samples using Pt as the co-catalyst

| Catalysts | Surface area (m ² g ⁻¹) | Incident light (λ) | Reaction solution | H ₂ evolution (μmol h ⁻¹) |
|---|--|--------------------|-------------------|--|
| 3 wt% | 160 | ≥420 nm | Triethanolamine | 574 |
| Pt/NS-g-C ₃ N ₄ | | | | |
| 3 wt% | 10 | ≥420 nm | Triethanolamine | 12.5 |
| Pt/bulk g-C ₃ N ₄ | | | | |
| 3 wt% | 182 | ≥420 nm | Triethanolamine | 123 |
| Pt/mpg-C ₃ N ₄ | | | | |

approximately 2 times more in comparison to pure g-C₃N₄ (14 μmol h⁻¹). The photocurrent generation for I-doped g-C₃N₄ was also nearly 3 times higher than that of pure g-C₃N₄, which explains the increased mobility of the photogenerated charge carriers. As compared to undoped g-C₃N₄, the P-doped g-C₃N₄ showed a significantly enhanced electrical conductivity of up to 4 orders of magnitude higher. It was also found that the photocurrent generation increased 5-fold.

6.3. Hydrogen production by noble metal-loaded g-C₃N₄

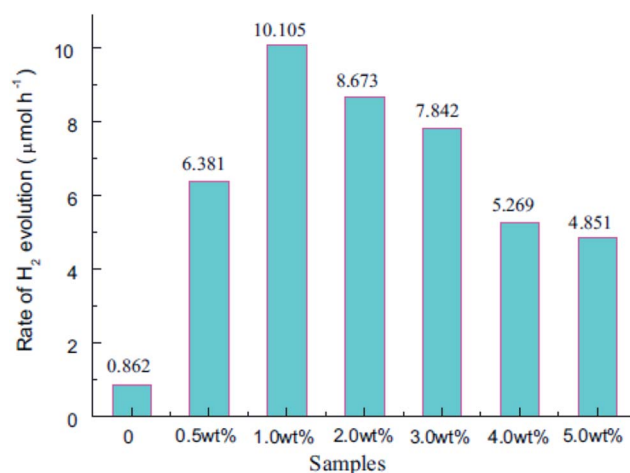
Among all the noble metals, platinum was found to be most efficient, with HER varying from 20 to 200 mmol h⁻¹ g⁻¹ depending on several factors, like the pH of the solution, the intensity of the light source, the selection of the sacrificial agent and the loading procedure of the co-catalyst. The HER increases with increasing Pt content to around 2–4%, and then it decreases. The deposition of Pt nanoparticles enhances the H₂ production, and the HER was about 172 μmol h⁻¹, which is 7 times more than that of neat g-C₃N₄ when the catalyst is synthesized from an organo sulphur compound and calcined at 550 °C, which indicates that the presence of S during calcination controls the polymerization and hence enhances its photocatalytic activity. Photocatalytic H₂ evolution using⁶⁵ Pt as a co-catalyst showed a value of 574 μmol h⁻¹ for 3 wt% Pt/NS-g-C₃N₄, whereas for 3 wt% Pt/bulk g-C₃N₄ it was only 12.5 μmol h⁻¹ and for 3 wt% Pt/mpg-C₃N₄ with a surface area of 182 m² g⁻¹, the H₂ evolution rate was found to be 123 μmol h⁻¹, as shown in Table 4.

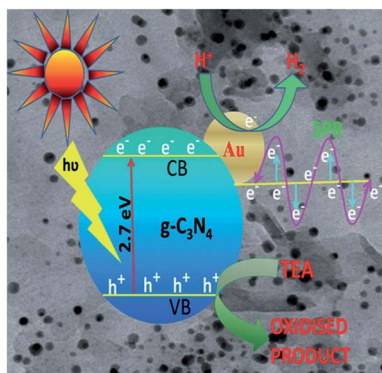
Table 5 Comparative study of the hydrogen evolution rates of the g-C₃N₄ samples synthesized at different processing temperatures using Pt as a co-catalyst

| Catalyst | Surface area (m ² g ⁻¹) | Incident light (λ) | Reaction solution | H ₂ evolution (μmol h ⁻¹) |
|---------------------------------|--|--------------------|-------------------|--|
| g-C ₃ N ₄ | 9 | ≥420 nm | Triethanolamine | 10 |
| CN-550 | 4 | ≥420 nm | Triethanolamine | 5 |
| CN-600 | 9 | ≥420 nm | Triethanolamine | 14 |
| CN-625 | 15 | ≥420 nm | Triethanolamine | 30 |
| CN-650 | 20 | ≥420 nm | Triethanolamine | 63 |
| CN-675 | 68 | ≥420 nm | Triethanolamine | 147 |
| CN-700 | 99 | ≥420 nm | Triethanolamine | 177 |

When hollow carbon nitride nanospheres were synthesized by grafting the organic group ATCN (2-aminothiophene-3-carbonitrile) into the structure of g-C₃N₄, the photocatalytic activity towards H₂ evolution increased 3-fold (278 μmol h⁻¹) by using Pt (3 wt%).⁴⁴ With the increase in the amount of the added organic compound, the sample also showed a red-shift from 420 nm to 700 nm. When Pt was doped on exfoliated g-C₃N₄ nanosheets,⁴⁰ the surface area of the material was as high as 384 m² g⁻¹, and it contained an ample number of nitrogen-containing active sites, which are favourable for enhancing its photocatalytic activity. The photocatalytic HER of Pt-doped g-C₃N₄ nanosheets was found to be 93 μmol h⁻¹, which is much higher than that of neat g-C₃N₄ (10 μmol h⁻¹). When 3 wt% of Pt was loaded onto the surface of the catalyst by an *in situ* photo-deposition method, the HER of the sample was found to be dependent on the processing temperature. When the processing temperature was below 650 °C, the absorption edge was blue-shifted, but when it was above 650 °C, the band edge was slightly red-shifted (Table 5).

Pt-doped hollow mpg-C₃N₄ nanospheres (with a decreased shell thickness of the nanospheres of 10–30 nm) showed enhanced photocatalytic hydrogen evolution due to increased light absorption in the visible region. The hollow CNS samples with 3 wt% of Pt as a co-catalyst showed a HER of 224 μmol h⁻¹, which is 25 times higher than that of the bulk. The photocatalytic activity was enhanced towards water splitting under visible light irradiation by incorporating Rh metal into the g-C₃N₄ network with the decrease of the particle size. When the size of the metallic Rh nanoparticles was around 9 nm, the hydrogen evolution rate increased, whereas when the size of the metallic Rh nanoparticles was around 25–50 nm, Rh particles were preferred as catalysts for the oxidation reaction (CH₄ + 2H₂O → CO₂ + 8H).⁶⁷ The added Rh nanoparticles with particle sizes ranging from 1 to 5 nm behave as efficient photocatalysts for water splitting to produce hydrogen in the presence of methanol as the sacrificial agent. The H₂ production rate of

**Fig. 22** Photocatalytic activity of Ag/g-C₃N₄ composites for H₂ evolution from methanol solution under visible light (reproduced from ref. 61).



Scheme 7 Mechanism of photocatalytic hydrogen production and surface plasmon resonance of Au in an Au/C₃N₄ nanocomposite (reproduced from ref. 70).

the most active catalyst, Rh(PVP)/C₃N₄, was 60 μmol during a reaction time of 4 h. When the Rh particles become larger, the H₂ production rate is significantly decreased. Hence, the photodeposition method is the preferred method to deposit nanoparticles on the surface of g-C₃N₄. Lei *et al.*⁶¹ reported that with an increase in Ag loading, the H₂ production rate was found to increase. The neat g-C₃N₄ sample showed a HER of 0.862 μmol h⁻¹ g⁻¹ under visible light, whereas after Ag loading H₂ evolution rate was 10.105 μmol h⁻¹ g⁻¹, which was about 11.7 times more than that of neat g-C₃N₄. An optimum (1.0 wt%) Ag loading results in good dispersion on the surface of g-C₃N₄, which enhances the photocatalytic activity of the composite significantly, as shown in Fig. 22.

However, in Ag₂S-modified g-C₃N₄ composite, the photocatalyst shows a significantly improved H₂ production compared to that of pristine g-C₃N₄ in the range of 460 to 490 nm, which is around 100 times than that of pure g-C₃N₄.⁶¹ The maximum activity was observed with 5 wt% Ag₂S-g-C₃N₄ when the size of the Ag₂S nanoparticles were 8 to 16 nm. Also the H₂ evolution was about 532.2 μmol when the reaction was performed under visible light illumination (λ > 400 nm). The optimum 1 wt% AuNPs-loaded g-C₃N₄ produced 23 times⁷¹ more H₂ gas than neat g-C₃N₄. However, when doubling the concentration of the AuNPs, the amount of H₂ gas production decreased to nearly half that value. The mechanism of photocatalytic hydrogen production and the surface plasmon resonance of Au in the Au/C₃N₄ nanocomposite is presented in Scheme 7. As the Fermi level of the Au NPs exists between the conduction band maximum and the valence band minimum of

the polar semiconducting material, the surface wave can propagate easily at the interface between the g-C₃N₄ and Au NPs, resulting in the formation of plasmonic photocatalysts, and hence the photocatalytic performance of g-C₃N₄ can be further improved.

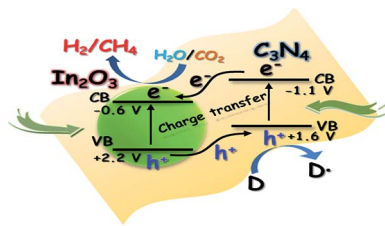
A comparative study of the synthesis methods and the activity over noble metal-doped g-C₃N₄ is presented in Table 6.

6.4. Hydrogen production by transition metal- and metal oxide-based composites and heterojunctions with g-C₃N₄

Sun *et al.*⁸⁰ reported that Zn/g-C₃N₄ shows a red-shift in the absorption edge, and the new organic metal hybrid material shows a 10 times higher rate of photocatalytic H₂ evolution under visible light. The synergistic combination of the enhanced specific surface area, the crystalline anatase phase, the small crystallite size, the effective charge separation and enhanced visible light absorption ability makes the N,S-TiO₂/g-C₃N₄ photocatalyst effective for photocatalytic H₂ evolution under visible light irradiation. Because of the faster recombination of photogenerated charge carriers, the amount of hydrogen evolution (125 μmol h⁻¹) in neat g-C₃N₄ is limited. However, in the⁸⁴ N,S-TiO₂/g-C₃N₄ photocatalyst comparison to neat g-C₃N₄, there could be seen an enhanced activity towards H₂ evolution. As the wt% of thiourea (*i.e.* from 1 to 10) is increased, gradually the H₂ evolution rate increases (*i.e.* from 161 to 317 μmol h⁻¹). According to Zhou *et al.*,⁸⁹ by preparing a Cu(OH)₂/g-C₃N₄ composite, the photocatalyst showed a higher H₂-production rate (48.7 μmol h⁻¹ g⁻¹), which was 16.5 times greater than that of pure g-C₃N₄. In₂O₃-g-C₃N₄ hybrids are used as efficient photocatalysts for H₂ generation and CO₂ reduction, rather than pure In₂O₃ and g-C₃N₄, as the pure In₂O₃ shows no noticeable H₂ evolution,⁹³ while the pure g-C₃N₄ shows a H₂ generation rate of only 0.19 μmol h⁻¹; whereas In₂O₃-g-C₃N₄ (10 wt%) hybrid exhibits a 5 times higher H₂ generation rate (0.99 μmol h⁻¹) than pure g-C₃N₄. However, an increase in the concentration of In₂O₃ nanocrystals (>10 wt%) on the g-C₃N₄ surfaces results in a decrease in photocatalytic activity for H₂ generation. The photocatalytic CO₂ reduction into hydrocarbon fuels is also a promising application of the In₂O₃-g-C₃N₄ hybrid photocatalyst. The In₂O₃-g-C₃N₄ hybrid photocatalyst has exhibited a CH₄ production more than 3 times higher than that of neat g-C₃N₄ and more than 4 times higher than that of neat In₂O₃, with an optimum concentration of 10 wt% In₂O₃. The mechanism of charge transfer in the In₂O₃-g-C₃N₄ hybrid photocatalyst is presented in Scheme 8.

Table 6 Comparative study of the synthesis methods and hydrogen evolution over noble metal-doped g-C₃N₄

| Noble metal | Reagent used | Synthesis method | Catalyst | Incident light (λ) | Reaction solution | H ₂ evolution (μmol h ⁻¹ g ⁻¹) | Reference |
|-------------|--|---------------------------------|--|--------------------|-------------------|--|-----------|
| Ag | AgNO ₃ | Facile heating method | 1 wt% Ag/g-C ₃ N ₄ | ≥420 nm | Methanol | 10.105 | 61 |
| Au | HAuCl ₄ , AuCl ₃ | Deposition-precipitation method | 1 wt% Au/g-C ₃ N ₄ | ≥400 nm | Triethanolamine | 532 | 70 |
| Pt | H ₂ PtCl ₄ | Deposition-method | 1 wt% Pt/g-C ₃ N ₄ | ≥420 nm | Triethanolamine | 732 | 44 |
| Rh | RhCl ₃ ·nH ₂ O | Polyol reduction method | Rh(PVP)/g-C ₃ N ₄ -4 : 1 | 420–630 nm | Methanol | 14.9 | 67 |



Scheme 8 Schematic of charge transfer in $\text{In}_2\text{O}_3\text{-g-C}_3\text{N}_4$ (reproduced from ref. 93, licence number 3767471444007).

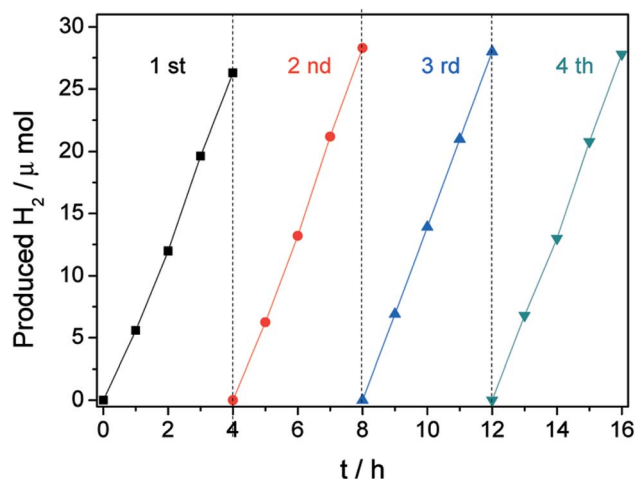


Fig. 23 Long-term H_2 evolution by a $\text{Ni/NiO/C}_3\text{N}_4$ nanocomposite under visible light (reproduced from ref. 96, licence number 3767480083704).

Zhang *et al.*⁹⁶ also studied the photocatalytic activity of $\text{Ni/NiO-g-C}_3\text{N}_4$ composites and found that Ni/NiO nanoparticles were properly dispersed on the surface of $\text{g-C}_3\text{N}_4$, indicating a strong

interaction between Ni/NiO nanoparticles and the soft interface of the polymeric C_3N_4 , thus promoting the surface kinetics by the channelization of the photoelectrons and hindering the recombination rate. The generated photoelectrons are first transferred to the Ni -core surface and then to the NiO shell and therefore speeding up the catalytic reaction, leading to a much higher HER compared to neat $\text{g-C}_3\text{N}_4$. In $\text{Ni/NiO-g-C}_3\text{N}_4$ (1 wt%), the HER is enhanced to $5 \mu\text{mol h}^{-1}$. But after 4 h of visible light irradiation, the HER increases to $40 \mu\text{mol h}^{-1}$. However, further increases in the Ni/NiO wt% decreases the photocatalytic activity and HER, although the long-term H_2 evolution shows no decrease in the activity of 2 wt% Ni/NiO modified $\text{g-C}_3\text{N}_4$ as shown in Fig. 23. The hydrogen evolution data of various metallic elements and metal oxides heterojunctions with $\text{g-C}_3\text{N}_4$ is represented in Table 7.

7. Summary and outlook

The present review summarized the recent development on $\text{g-C}_3\text{N}_4$ -based photocatalysts for efficient hydrogen generation under visible light irradiation. It is concluded that the visible light photocatalytic performance of $\text{g-C}_3\text{N}_4$ can be significantly improved by careful design of the nanostructure and nanoporous structure, by bandgap engineering, by surface functionalization with noble metals, non-metals and transition metals and by heterojunction construction. Although energy band engineering has been widely studied to modify the optical property of $\text{g-C}_3\text{N}_4$, further efforts are still being made to achieve the desired efficiency. More research is still required to modify the band structure, porous network and crystallinity of $\text{g-C}_3\text{N}_4$ to achieve a significant quantum yield for hydrogen production. The main drawback in $\text{g-C}_3\text{N}_4$ research lies with the high electron-hole recombination at the surface of $\text{g-C}_3\text{N}_4$, which limits its potential application. Therefore, the combination of energy band engineering with other modification strategies, such as

Table 7 Summaries of various metallic elements and metal oxide heterojunctions with $\text{g-C}_3\text{N}_4$ for hydrogen evolution

| Metal/metal oxide | Precursor | Synthesis method | Photocatalysts | Incident light (λ) | Reaction solution | H_2 evolution ($\mu\text{mol g}^{-1} \text{h}^{-1}$) | Reference |
|--|--|--|--|------------------------------|---|---|-----------|
| Ti | TiO_2 and $\text{g-C}_3\text{N}_4$ | Solid-state pyrolysis | 50 wt% $\text{TiO}_2/\text{g-C}_3\text{N}_4$ | $\geq 436 \text{ nm}$ | Methanol | Pt/22.4 | 81 |
| Zn | (1) $\text{Zn}(\text{NO}_3)_2 \cdot 6\text{H}_2\text{O}$ (2) $\text{Zn}(\text{CH}_3\text{COO})_2$ | Post-annealing solid-state pyrolysis | 10% $\text{Zn/g-C}_3\text{N}_4$ | $\geq 420 \text{ nm}$ | Methanol | 59.5 | 80 |
| CeO ₂ | $(\text{NH}_4)_2\text{Ce}(\text{NO}_3)_6$ | Solid-state reaction | 8% $\text{CeO}_2/\text{g-C}_3\text{N}_4$ | $\geq 420 \text{ nm}$ | Lactate solution | 73.12 | 128 |
| Sn | (i) $\text{SnCl}_4 \cdot 5\text{H}_2\text{O}$ in methanol (ii) K_2SnO_3 in ethanol | Ultrasonic deposition | 47.5% $\text{SnO}_2\text{-g-C}_3\text{N}_4/\text{SnO}_2\text{-Pt}$ | $\geq 420 \text{ nm}$ | Triethanol-amine | 900 | 82 |
| N,S-TiO ₂ | $\text{TiOSO}_4 \cdot x\text{H}_2\text{O}$ and thiourea | Thermal polymerization | 10% $\text{N,S-TiO}_2/\text{g-C}_3\text{N}_4$ | $\geq 400 \text{ nm}$ | Methanol | 317 | 84 |
| FeOx modified $\text{g-C}_3\text{N}_4$ | Ferrocene and urea | One-step calcination | 100 $\text{FeOx/g-C}_3\text{N}_4$ (100 Fe-CN) | $\geq 420 \text{ nm}$ | Triethanol-amine | 108 | 87 |
| MoS ₂ | MoS_2 | Solid-state reaction | 3% $\text{MoS}_2/\text{g-C}_3\text{N}_4$ | $\geq 420 \text{ nm}$ | 0.1 M Na_2SO_4 solution | 50 | 91 |
| Cu | (1) $\text{Cu}(\text{CH}_3\text{COO})_2 \cdot \text{H}_2\text{O}$ (2) $\text{Cu}(\text{NO}_3)_2$ (3) CuCl_2 and NaOH | Chemical precipitation Hydrothermal precipitation | 0.34 mol%, $\text{Cu}(\text{OH})_2/\text{g-C}_3\text{N}_4$ | $\geq 400 \text{ nm}$ | Methanol | 48.7 | 89 |
| In_2O_3 | $\text{In}(\text{AO})_3 + \text{g-C}_3\text{N}_4$ | Simple solvothermal | 10 wt% $\text{In}_2\text{O}_3/\text{g-C}_3\text{N}_4$ | $\geq 420 \text{ nm}$ | 0.1 M L-ascorbic acid | 0.99 | 93 |
| NiO | $\text{Ni}(\text{NO}_3)_2 \cdot 6\text{H}_2\text{O}$ | Direct reduction | 2 wt% $\text{Ni/g-C}_3\text{N}_4$ | $\geq 420 \text{ nm}$ | Triethanol-amine | 10 | 96 |

noble metal loading/heterojunction formation, is highly encouraged to find superior ways to improve the performance of g-C₃N₄. Also further research on the surface activation of g-C₃N₄ for the purpose of the specific binding of functional groups to modify the light absorbing property in higher wavelengths is highly necessary. The potential applications of g-C₃N₄ can also be further extended to a wide range of heterogeneous catalysis for various reactions, like artificial photosynthesis for significant CO₂ reduction to generate hydrocarbon fuels, as a reactive template for metal nitride synthesis, in nanocasting to obtain a special nanostructure, as electrocatalysts for fuel cells, in lithium ion batteries, and in sensors and solar cell applications.

Acknowledgements

The authors are highly obliged to the president of ITER, S'O'A University for the financial support for carrying out the work.

References

- J. Zhang, X. Chen, K. Takanebe, K. Maeda, K. Domen and J. D. Epping, *Angew. Chem., Int. Ed.*, 2010, **49**, 441–444.
- J. J. Zhu, Y. C. Wei, W. K. Chen, Z. Zhao and A. Thomas, *Chem. Commun.*, 2010, **46**, 6965.
- S. Martha, A. Nasim and K. M. Parida, *J. Mater. Chem. A*, 2013, **1**, 7816–7824.
- P. W. J. Wang, J. Zhao, L. Guo and F. E. Osterloh, *J. Mater. Chem. A*, 2014, **2**, 20338–20344.
- D. J. Martin, K. Qiu, S. A. Shevlin, A. D. Handoko, X. Chen, Z. Guo and J. Tang, *Angew. Chem., Int. Ed.*, 2014, **53**, 9240–9245.
- B. Long, J. Lin and X. Wang, *J. Mater. Chem. A*, 2014, **2**, 2942.
- Y. Cui, Z. Ding, X. Fu and X. Wang, *Angew. Chem., Int. Ed.*, 2012, **51**, 118.
- J. Liebig, *Ann. Pharm.*, 1834, **10**, 10.
- E. C. Franklin, *J. Am. Chem. Soc.*, 1922, **44**, 486.
- Y. Wan and D. Y. Zhao, *Chem. Rev.*, 2007, **107**, 2821.
- A. Thomas, A. Fischer, F. Goettmann, M. Antonietti, J. O. Muller, R. Schloglb and J. M. Carlssonc, *J. Mater. Chem.*, 2008, **18**, 4893.
- C. Li, X. Yang, B. Yang, Y. Yan and Y. Qian, *Mater. Chem. Phys.*, 2007, **103**, 427.
- F. Goettmann, A. Thomas and M. Antonietti, *Angew. Chem., Int. Ed.*, 2007, **46**, 2717.
- X. B. Chen, S. H. Shen, L. J. Guo and S. S. Mao, *Chem. Rev.*, 2010, **110**, 6503.
- R. M. N. Yerga, M. C. A. Galvan, F. del Valle, J. A. V. de la Mano and J. L. Fierro, *ChemSusChem*, 2009, **2**, 471.
- Y. Zheng, L. Lin, X. Ye, F. Guo and X. Wang, *Angew. Chem., Int. Ed.*, 2014, **53**, 11926–11930.
- S. W. Bian, Z. Ma and W. G. Song, *J. Phys. Chem. C*, 2009, **113**, 8668–8672.
- G. Zhang, J. Zhang, M. Zhang and X. Wang, *J. Mater. Chem.*, 2012, **22**, 8083.
- X. X. Zou, G. D. Li, Y. N. Wang, J. Zhao, C. Yan, M. Y. Guo, L. Li and J. S. Chen, *Chem. Commun.*, 2011, **47**, 1066.
- Y. Guo, S. Chu, S. Yan, Y. Wang and Z. Zou, *Chem. Commun.*, 2010, **7**, 325.
- X. C. Wang, K. Maeda, A. Thomas, K. Takanebe, G. Xin, K. Domen and M. Antonietti, *Nat. Mater.*, 2009, **8**, 76.
- Y. Zhang, Q. Pan, G. Chai, M. Liang, G. Dong, Q. Zhang and J. Qiu, *Sci. Rep.*, 2013, **3**, 1943.
- M. Mattesini, S. F. Matar, A. Snis, J. Etourneau and A. Mavromaras, *J. Mater. Chem.*, 1999, **9**, 3151.
- M. Mattesini, S. F. Matar and J. Etourneau, *J. Mater. Chem.*, 2000, **10**, 709.
- Q. X. Guo, Y. Xie, X. J. Wang, S. C. Lv, T. Hou and X. M. Liu, *Chem. Phys. Lett.*, 2003, **380**, 84.
- X. C. Wang, K. Maeda, X. F. Chen, K. Takanebe, K. Domen, Y. D. Hou, X. Z. Fu and M. Antonietti, *J. Am. Chem. Soc.*, 2009, **131**, 1680–1681.
- Y. Zheng, J. Liu, J. Liang, M. Jaroniecc and S. Z. Qiao, *Energy Environ. Sci.*, 2012, **5**, 6717–6731.
- A. Taguchi and F. Sch€uth, *Microporous Mesoporous Mater.*, 2005, **77**, 1.
- J. Wang, C. Zhang, Y. Shen, Z. Zhou, J. Yu, Y. Li, W. Wei, S. Liu and Y. Zhang, *J. Mater. Chem. A*, 2015, **3**, 5126–5131.
- H. Yan, *Chem. Commun.*, 2012, **48**, 3430–3432.
- X. Chen, Y. S. Jun, K. Takanebe, M. Kazuhiko, K. Domen, F. Xianzhi, A. Markus and X. Wang, *Chem. Mater.*, 2009, **21**, 4093–4095.
- Z. Wang, W. Guan, Y. Sun, F. Dong, Y. Zhouc and W. K. Ho, *Nanoscale*, 2015, **7**, 2471–2479.
- S. Kumar, T. Surendar, B. Kumar, A. Baruah and V. Shanker, *RSC Adv.*, 2014, **4**, 8132–8137.
- Y. Wang, X. C. Wang and M. Antonietti, *Angew. Chem., Int. Ed.*, 2012, **51**, 68–89.
- Z. Yang, Y. Zhang and Z. Schnepf, *J. Mater. Chem. A*, 2015, **3**, 14081–14092.
- X. F. Chen, J. S. Zhang, X. Fu, M. Antonietti and X. C. Wang, *J. Am. Chem. Soc.*, 2009, **131**, 11658–11659.
- Y. S. Jun, W. H. Hong, M. Antonietti and A. Thomas, *Adv. Mater.*, 2009, **21**, 4270–4274.
- M. Groenewolt and M. Antonietti, *Adv. Mater.*, 2005, **17**, 1789–1792.
- X. Bai, L. Wang, R. Zong and Y. Zhu, *J. Phys. Chem. C*, 2013, **117**, 9952–9961.
- S. Yang, Y. Gong, J. Zhang, L. Zhan, L. Ma, Z. Fang, R. Vajtai, X. Wang and P. M. Ajayan, *Adv. Mater.*, 2013, **25**, 2452–2456.
- F. Cheng, H. Wang and X. Dong, *Chem. Commun.*, 2015, **51**, 7176.
- Y. Chen, B. Wang, S. Lin, Y. Zhang and X. Wang, *J. Phys. Chem. C*, 2014, **118**, 29981–29989.
- D. Zheng, C. Pang, Y. Liu and X. Wang, *Chem. Commun.*, 2015, **51**, 9706–9709.
- D. Zheng, C. Huang and X. Wang, *Nanoscale*, 2015, **7**, 465.
- X. Bai, J. Lee, C. Cao and S. Hussain, *Mater. Lett.*, 2011, **65**, 1101.
- Y. Chen, J. Zhang, M. Zhang and X. Wang, *Chem. Sci.*, 2013, **4**, 3244.
- Y. Wang, Y. Di, M. Antonietti, H. Li, X. Chen and X. Wang, *Chem. Mater.*, 2010, **22**, 5119–5121.

- 48 Z. Lin and X. Wang, *ChemSusChem*, 2014, **6**, 1547.
- 49 Y. Wang, H. Li, J. Yao, X. Wanga and M. Antonietti, *Chem. Sci.*, 2011, **2**, 446–450.
- 50 X. Ma, L. Yanhui, J. Xu, Y. Liu, R. Zhang and Y. Zhu, *J. Phys. Chem. C*, 2012, **116**, 23485–23493.
- 51 S. C. Yan, Z. S. Li and Z. G. Zou, *Langmuir*, 2010, **26**, 3894–3901.
- 52 Y. Zhang, T. Mori, J. Ye and M. Antonietti, *J. Am. Chem. Soc.*, 2010, **132**, 6294–6295.
- 53 G. Dong, K. Zhao and L. Zhang, *Chem. Commun.*, 2012, **48**, 6178–6180.
- 54 J. S. Zhang, X. F. Chen, K. Takanaabe, K. Maeda, K. Domen, J. D. Epping, X. Z. Fu, M. Antonietti and X. C. Wang, *Angew. Chem., Int. Ed.*, 2010, **49**, 441–444.
- 55 G. Liu, P. Niu, C. Sun, S. C. Smith, Z. Chen, G. Qing (Max) Lu and H. M. Cheng, *J. Am. Chem. Soc.*, 2010, **132**, 11642–11648.
- 56 J. Hong, X. Xia, Y. Wang and R. Xu, *J. Mater. Chem.*, 2012, **22**, 15006–15012.
- 57 G. Zhang, M. Zhang, X. Ye, X. Qiu, S. Lin and X. Wang, *Adv. Mater.*, 2014, **26**, 805–809.
- 58 J. Zhang, X. Chen, K. Takanaabe, K. Maeda, K. Domen, J. D. Epping, X. Fu, M. Antonietti and X. Wang, *Angew. Chem., Int. Ed.*, 2010, **48**, 451.
- 59 F. J. Zhang, F. Z. Xie, S. F. Zhu, J. Liu, J. Zhang, S. F. Mei and W. Zhao, *Chem. Eng. J.*, 2013, **228**, 435–441.
- 60 D. Jiang, L. Chen, J. Xie and M. Chen, *Dalton Trans.*, 2014, **43**, 4878–4885.
- 61 L. Ge, C. Han, J. Liu and Y. Li, *Appl. Catal., A*, 2011, **409–410**, 215–222.
- 62 L. Shi, L. Liang, J. Ma, F. Wang and J. Sun, *Catal. Sci. Technol.*, 2014, **4**, 758–765.
- 63 S. Meng, X. Ning, T. Zhang, S. F. Chen and X. Fu, *Phys. Chem. Chem. Phys.*, 2015, **17**, 11577–11585.
- 64 P. He, L. Song, S. Zhang, X. Wu and Q. Wei, *Mater. Res. Bull.*, 2014, **51**, 432–437.
- 65 J. H. Zeng and J. Y. Lee, *J. Power Sources*, 2005, **140**, 268–273.
- 66 G. Zhang, Z. Lan, L. Lin, S. Lin and X. Wang, *Chem. Sci.*, 2016, **7**, 3062–3066.
- 67 Y. Zhang, D. A. J. Michel Lighthart, X. Y. Quek, L. Gao and E. J. M. Hensen, *Int. J. Hydrogen Energy*, 2014, **39**, 11537–11546.
- 68 X. Y. Quek, Y. Guan and E. Hensen, *Catal. Today*, 2012, **183**, 72–78.
- 69 T. Ikeda, A. Xiong, T. Yoshinaga, K. Maeda, K. Domen and T. Teranishi, *J. Phys. Chem. C*, 2013, **117**, 2467–2473.
- 70 S. Samanta, S. Martha and K. M. Parida, *ChemCatChem*, 2014, **6**, 1453–1462.
- 71 S. Chang, A. Xie, S. Chen and J. Xiang, *J. Electroanal. Chem.*, 2014, **719**, 86–91.
- 72 J. Zhuang, W. Lai, M. Xu, Q. Zhou and D. Tang, *ACS Appl. Mater. Interfaces*, 2015, **7**(15), 8330–8338.
- 73 X. H. Li, X. Wang and M. Antonietti, *Chem. Sci.*, 2012, **3**, 2170.
- 74 N. Chang, J. Tian, Q. Liu, C. Ge, A. H. Qusti, A. M. Asiri, A. O. A. Yousi and X. Sun, *ACS Appl. Mater. Interfaces*, 2013, **5**, 6815–6819.
- 75 C. Chang, Y. Fu, M. Hu, C. Wang, G. Shan and L. Zhu, *Appl. Catal., B*, 2013, **142**, 553–560.
- 76 Y. Wang, J. Yao, H. Li, D. Su and M. Antonietti, *J. Am. Chem. Soc.*, 2011, **133**, 2362–2365.
- 77 H. Dai, X. Gao, E. Liu, Y. H. Yang, W. Q. Hou, L. M. Kang, J. Fan and X. Hu, *Diamond Relat. Mater.*, 2013, **38**, 109–117.
- 78 C. Langhammer, Z. Yuan, I. Zorić and B. Kasemo, *Nano Lett.*, 2006, **6**, 833–838.
- 79 Y. Xiong, B. Wiley, J. Chen, Z. Y. Li, Y. Yin and Y. Xia, *Angew. Chem., Int. Ed.*, 2005, **44**, 7913–7917.
- 80 J. K. Sun, Y. P. Yuan, L. G. Qiu, X. Jiang, A. J. Xie, Y. H. Shena and J. F. Zhub, *Dalton Trans.*, 2012, **41**, 6756–6763.
- 81 H. Yan and H. Yang, *J. Alloys Compd.*, 2011, **509**, 26–29.
- 82 R. Yin, Q. Luo, D. Wang, H. Sun, Y. Li, X. Li and J. An, *J. Mater. Sci.*, 2014, **49**, 6067–6073.
- 83 Y. Wang, B. Li, C. Zhang, L. Cui, S. Kang, X. Li and L. Zhou, *RSC Adv.*, 2013, **3**, 22269–22279.
- 84 S. Pany and K. M. Parida, *Phys. Chem. Chem. Phys.*, 2015, **17**, 8070–8077.
- 85 S. Hu, R. Jin, G. Lu, D. Liub and J. Gu, *RSC Adv.*, 2014, **4**, 24863–24869.
- 86 X. Chen, J. Zhang, X. Fu, M. Antonietti and X. Wang, *J. Am. Chem. Soc.*, 2009, **131**, 11658–11659.
- 87 R. Cheng, L. Zhang, X. Fan, M. Wang, M. Li and J. Shi, *Carbon*, 2016, **101**, 62–70.
- 88 B. Peng, S. Zhang, S. Yang, H. Wang, H. Yu, S. Zhang and F. Peng, *Mater. Res. Bull.*, 2014, **56**, 19–24.
- 89 X. Zhou, L. Z. Zhihui, P. Tao, B. Jin, Z. Wu and Y. Huang, *Mater. Chem. Phys.*, 2014, **143**, 1462–1468.
- 90 Y. He, L. Zhang, X. Wang, Y. Wu, H. Lin, L. Zhao, W. Weng, H. Wan and M. Fan, *RSC Adv.*, 2014, **4**, 13610–13619.
- 91 T. Yuming, G. Lei, W. Kaiyue and C. Yueshenga, *Mater. Charact.*, 2014, **87**, 70–73.
- 92 A. T. Doan, D. X. Nguyen, T. P. H. Nguyen, T. V. N. Nguyen, S. J. Kim and V. Vo, *Bull. Korean Chem. Soc.*, 2014, **35**, 1794–1798.
- 93 S. W. Cao, X. F. Liu, Y. P. Yuan, Z. Y. Zhang, Y. S. Liao, J. Fang, S. C. J. Loo, T. C. Sum and C. Xue, *Appl. Catal., B*, 2014, **147**, 940–946.
- 94 G. Zhang, S. Zang and X. Wang, *ACS Catal.*, 2015, **5**, 941–947.
- 95 G. Zhang, C. Huang and X. Wang, *Small*, 2015, **11**, 1215.
- 96 G. Zhang, G. Li and X. Wang, *ChemCatChem*, 2015, **7**, 2864–2870.
- 97 J. Shi, J. Chen, Z. Feng, T. Chen, Y. Lian, X. Wang and C. Li, *J. Phys. Chem. C*, 2007, **111**, 693.
- 98 J. Jitputti, T. Rattanavoravipa, S. Chuangchote, S. Pavasupree, Y. Suzuki and S. Yoshikawa, *Catal. Commun.*, 2009, **10**, 378.
- 99 X. Lu, G. Wang, S. Xie, J. Shi, W. Li, Y. Tong and Y. Li, *Chem. Commun.*, 2012, **48**, 7717–7719.
- 100 G. R. Bamwenda, T. Uesigi, Y. Abe, K. Sayama and H. Arakawa, *Appl. Catal., A*, 2001, **205**, 117.

- 101 J. Kim, D. Hwang, H. G. Kim, S. W. Bae, J. S. Lee, W. Li and S. H. Oh, *Top. Catal.*, 2005, **35**, 295.
- 102 K. Domen, S. Naito, W. M. Som, T. Onishi and K. Tamaru, *J. Chem. Soc., Chem. Commun.*, 1980, 543.
- 103 H. Kato, K. Asakura and A. Kudo, *J. Am. Chem. Soc.*, 2003, **125**, 3082.
- 104 A. Kudo and H. Kato, *Chem. Phys. Lett.*, 2000, **331**, 373.
- 105 H. Kadowaki, N. Saito, H. Nishiyama, H. Kobayashi, Y. Shimodaira and Y. Inoue, *J. Phys. Chem. C*, 2007, **111**, 439.
- 106 N. Saito, H. Kadowaki, H. Kobayashi, K. Ikarashi, H. Nishiyama and Y. Inoue, *Chem. Lett.*, 2004, **33**, 1452.
- 107 J. Yu, Y. Zhang and A. Kudo, *J. Solid State Chem.*, 2009, **182**, 223.
- 108 J. S. Jang, U. A. Joshi and J. S. Lee, *J. Phys. Chem. C*, 2007, **111**, 13280.
- 109 N. Bao, L. Shen, T. Takata, D. Lu and K. Domen, *Chem. Lett.*, 2006, **35**, 318.
- 110 N. Bao, L. Shen and T. Takata, *Chem. Mater.*, 2008, **20**, 110.
- 111 X. Fu, X. Wang, Z. Chen, Z. Zhang, Z. Li, D. Y. C. Leung, L. Wu and X. Fu, *Appl. Catal., B*, 2010, **95**, 393.
- 112 Z. Lei, W. You, M. Liu, G. Zhou, T. Takata, M. Hara, K. Domen and C. Li, *Chem. Commun.*, 2003, **17**, 2142.
- 113 J. S. Jang, S. H. Choi, N. Shin, C. Yu and J. S. Lee, *J. Solid State Chem.*, 2007, **180**, 1110.
- 114 M. Tabata, K. Maeda, T. Ishihara, T. Minegishi, T. Takata and K. Domen, *J. Phys. Chem. C*, 2010, **114**, 11215–11219.
- 115 G. Wang, B. Huang, Z. Li, Z. Lou, Z. Wang, Y. Dai and M. H. Whangbo, *Sci. Rep.*, 2015, **5**, 8544.
- 116 B. B. Kale, J. O. Baeg, S. M. Lee, H. Chang, S. J. Moon and C. W. Lee, *Adv. Funct. Mater.*, 2006, **16**, 1349.
- 117 L. Zheng, Y. Xu, Y. Song, C. Wu, M. Zhang and Y. Xie, *Inorg. Chem.*, 2009, **48**, 4003.
- 118 W. Xiao, J. Yuan, Y. Zhang and W. Shangguan, *Mater. Chem. Phys.*, 2007, **105**, 6.
- 119 M. Hara, G. Hitoki, T. Takata, J. N. Kondo, H. Kobayashi and K. Domen, *Catal. Today*, 2003, **78**, 555.
- 120 K. Maeda, K. Teramura, N. Saito, Y. Inoue and K. Domen, *Bull. Chem. Soc. Jpn.*, 2007, **80**, 1004.
- 121 N. Arai, N. Saito, H. Nishiyama, Y. Inoue, K. Domen and K. Sato, *Chem. Lett.*, 2006, **35**, 796.
- 122 M. Hara, T. Takata, J. N. Kondo and K. Domen, *Catal. Today*, 2004, **90**, 313.
- 123 A. Kasahara, K. Nukumizu, T. Takata, J. N. Kondo, M. Hara, H. Kobayashi and K. Domen, *J. Phys. Chem. B*, 2003, **107**, 791.
- 124 M. Liu, W. You, Z. Lei, G. Zhou, J. Yang, G. Wu, G. Ma, G. Luan, T. Takata, M. Hara, K. Domen and C. Li, *Chem. Commun.*, 2004, **19**, 2192.
- 125 T. Mishima, M. Matsuda and M. Miyake, *Appl. Catal., A*, 2007, **324**, 77.
- 126 K. Kamata, K. Maeda, D. Lu, Y. Kako and K. Domen, *Chem. Phys. Lett.*, 2009, **470**, 90.
- 127 Y. Xie, F. Wu, X. Sun, H. Chen, M. Lv, S. Ni, G. Liu and X. Xu, *Sci. Rep.*, 2016, **6**, 19060.
- 128 N. Tian, H. Huang, C. Liu, F. Dong, T. Zhang, X. Du, S. Yua and Y. Zhang, *J. Mater. Chem. A*, 2015, **3**, 17120–17129.
- 129 Y. Zang, L. Li, X. Li, R. Lin and G. Li, *Chem. Eng. J.*, 2014, **246**, 277–286.